



# **Measuring the Muon Neutrino Magnetic Moment in the NOvA Near Detector**

Róbert Králik

*Supervisor:* Dr. Lily Asquith

*A thesis submitted in fulfilment of the requirements for the degree of  
Doctor of Philosophy to the*

School of Mathematical and Physical Sciences  
University of Sussex

In Brighton, United Kingdom

August 6, 2024

I hereby declare that I carried out this thesis independently, and only with the cited sources, literature and other professional sources.

I also declare that this thesis has not been and will not be, submitted in whole or in part to another University for the award of any other degree.

*Brighton, United Kingdom,*

*August 6, 2024*

---

Róbert Králik

# Acknowledgements

School of Mathematical and Physical Sciences, University of Sussex

DOCTORAL THESIS

---

## Measuring the Muon Neutrino Magnetic Moment in the NOvA Near Detector

---

by Róbert Králik

### ABSTRACT

Measuring an enhanced neutrino magnetic moment would be a clear indication of physics beyond the Standard Model (BSM), shedding light on the correct BSM theory or the potential Majorana nature of neutrinos. It would manifest in the NOvA near detector as an excess of neutrino-on-electron elastic scattering interactions at low electron recoil energies. Leveraging an intense and highly pure muon neutrino beam, along with the finely segmented liquid scintillator detector technology specifically designed for electromagnetic shower separation, enables NOvA to achieve a potentially world-leading sensitivity in probing the effective muon neutrino magnetic moment. Despite facing statistical limitations stemming from the low cross section of the signal process, systematic uncertainties have a significant impact on this result. To address these challenges, the NOvA Test Beam experiment focuses on mitigating some of the largest systematic uncertainties within NOvA by investigating particle interactions and energy deposition in a small-scale replica NOvA detector. This thesis describes the calibration of the NOvA Test Beam detector, which is a crucial step in analysing the Test Beam data before they can be utilised to reduce NOvA systematic uncertainties. *COMMENT: Add final numbers for the analyses, also the POT and such*

Keywords: neutrino NOvA electromagnetic testbeam calibration

# Contents

<b>Acknowledgements</b>	<b>ii</b>
<b>List of Figures</b>	<b>v</b>
<b>List of Tables</b>	<b>vii</b>
<b>Preface</b>	<b>viii</b>
<b>1 Measuring the Muon Neutrino Magnetic Moment</b>	<b>1</b>
1.1 Theory of the Neutrino Magnetic Moment . . . . .	3
1.1.1 Neutrino Electric and Magnetic Dipole Moments . . . . .	5
1.1.2 Measuring the Neutrino Magnetic Moment . . . . .	8
1.2 Analysis Overview . . . . .	14
1.3 Event Selection . . . . .	17
1.3.1 Data Collection Quality . . . . .	18
1.3.2 Reconstruction Quality . . . . .	18
1.3.3 Pre-Selection . . . . .	20
1.3.4 Fiducial and Containment Cuts . . . . .	28
1.3.5 Multivariate Analysis Cuts . . . . .	29
1.4 Systematic Uncertainties . . . . .	44
1.5 Results . . . . .	48
1.6 Discussion . . . . .	53
1.7 Summary . . . . .	54
<b>Acronyms</b>	<b>56</b>
<b>Bibliography</b>	<b>58</b>

# List of Figures

1.1	Effective coupling of neutrinos with one photon electromagnetic field.	3
1.2	Neutrino-on-electron elastic scattering diagram . . . . .	8
1.3	Electron recoil energy versus recoil angle . . . . .	9
1.4	Comparison of the neutrino magnetic moment and Standard Model cross sections . . . . .	11
1.5	Ratio of the neutrino magnetic moment and Standard Model cross sections . . . . .	13
1.6	Vertex reconstruction quality cut . . . . .	21
1.7	Prong and hits reconstruction quality cuts . . . . .	22
1.8	Low calorimetric energy cut for reconstruction quality . . . . .	23
1.9	Number of hits cut for pre-selection . . . . .	25
1.10	Length of the longest prong cut for pre-selection . . . . .	26
1.11	$E\theta^2$ cut for pre-selection . . . . .	27
1.12	Vertex x containment cut . . . . .	30
1.13	Vertex y containment cut . . . . .	31
1.14	Vertex z containment cut . . . . .	32
1.15	Hit minimum x containment cut . . . . .	33
1.16	Hit maximum x containment cut . . . . .	34
1.17	Hit minimum y containment cut . . . . .	35
1.18	Hit maximum y containment cut . . . . .	36
1.19	Hit minimum z containment cut . . . . .	37
1.20	Hit maximum z containment cut . . . . .	38
1.21	Shower E fraction and number of hits cuts . . . . .	41
1.22	Reconstructed energy and $E\theta^2$ cuts . . . . .	42
1.23	NuoneID and EPi0ID cuts . . . . .	43
1.24	Background composition of final selection . . . . .	45
1.25	Summary of systematic uncertainties . . . . .	46
1.26	Neutrino flux systematic uncertainty . . . . .	46
1.27	Detector systematic uncertainties . . . . .	47
1.28	Final prediction and data comparison . . . . .	50

1.29 Fit results . . . . .	53
----------------------------	----

# List of Tables

1.1	Overview of the simulation samples and analysis weight used for the different signal and background components. . . . .	17
1.2	Event selection summary . . . . .	19
1.3	Event selection cutflow table for the reconstruction quality cuts . . .	24
1.4	Event selection cutflow table for the pre-selection . . . . .	28
1.5	Event selection cutflow table for the containment cuts . . . . .	29
1.6	Multivariate analysis cutflow table . . . . .	44
1.7	Interactions contributing to the SM background . . . . .	44



# Preface

In this Preface, I provide an overview of the research presented in this thesis, highlighting my personal contributions to the work presented in each chapter.

In chapter ?? I present an overview of the relevant literature of neutrinos and their place in the particle physics theory and experiments.

In chapter ?? I introduce the NOvA experiment, relying on publicly available information from published articles, theses, and presentations, as well as on internal NuMI Off-axis  $\nu_e$  Appearance (NOvA) documentation when a higher detail is required. This chapter presents a complete overview of the experiment's technical aspects relevant to either the measurement of the effective muon neutrino magnetic moment, or to the calibration of the NOvA Test Beam detector. This chapter is mainly a collection of work of my NOvA collaborators, their technical design reports for the NOvA experiment and official results. My only contribution to this chapter lies in the addition of new external measurements from the NA61 experiment, to improve the neutrino beam prediction in NOvA.

Chapter ?? details the calibration of the NOvA Test Beam detector, divided into three main sections.

Section ?? describes the Test Beam detector itself, as designed and constructed by my NOvA Test Beam experiment colleagues.

Section ?? presents the data-based simulation of cosmic muons used for the calibration, which originates as a simpler version of the simulation by my colleague. I then improved the event selection, implemented the energy and charge assignment, and produced and validated the simulation and the corresponding calibration samples.

Lastly, Sec. ?? describes the Test Beam detector calibration itself, which uses the NOvA codebase for calibration. I fully implemented the NOvA calibration

Chapter 1 describes the measurement of the effective muon neutrino magnetic moment. Introduces the experimental and theoretical context for the measurement, describes the details of the analysis, including the event selection and the systematic uncertainties and describes the results and discusses their implications.

Finally, chapter ?? concludes the findings of this thesis.

## **Data-based Simulation of Cosmic Muons**

I also inherited the first-version of the data-based simulation of cosmic muons for the Test Beam detector. However, this version of the simulation was just directly taken from the simulation of the muon-removed sample and did not work properly for the Test Beam detector.

I developed and validated the event selection of cosmic muons for the data-based simulation, implemented the energy and charge correction. I developed the data-based simulation of cosmic muons described in Sec. Specifically, I developed the event selection, implemented the energy and charge corrections, actually produced the simulation and the calibration samples, and validated them

## **Calibration of the NOvA Test Beam Detector**

The Test Beam detector calibration (Sec. ??) uses the same calibration techniques as are used for the other NOvA detectors. I inherited the Test Beam detector calibration when it was technically working, but not for simulation. Therefore, I was the first person to calibrate the simulated Test Beam detector and therefore complete the entire Test Beam detector calibration chain. This allowed for the first proper production of data for the Test Beam analysers. Starting from here, I included the fibre brightness for the Test Beam detector in the same way as is used for the Near and Far NOvA detectors (Sec. ??).

I implemented the NOvA calibration procedure in full for the Test Beam calibration, specifically adding the Fibre Brightness dependency and implementing it for all the data and simulation samples. I've created my own fibre brightness maps, my own threshold and shielding corrections (found out about the issue), improved the NOvA calibration code, made the attenuation fits for all the samples, did the same for absolute calibration, figured out there is a mistake in geometry, figured out we need to add the underfilled cells to the dead channels, changed the TS correction limits, improved the systematic uncertainty for the absolute calibration, validated the calibration, developed code for the validation

# Measurement of the Effective Muon Neutrino Magnetic Moment

I was just told its an interesting analysis, there was a previous NOvA thesis, but it wasn't very well developed, did not use the standard NOvA techniques and did not properly incorporate systematics into their fits/limits. From the ND group, I got the event classifier and the event selection, which however did not work very well for our signal. Additionally, I got the nuone and the nueccmec enhanced samples and the radiative correction weight from them. From NOvA in general I got the nominal ND sample and the data sample, the cross section and PPF weights and the fitting infrastructure in general. From the LDM analysis I got the general structure of the fitting framework.

I have done the literature review of what is the neutrino magnetic moment and what are its current limits and state of the art measurements. I designed the neutrino magnetic moment weight and developed my own event selection, including using the TMVA, which is not used elsewhere, and the general analysis infrastructure for the neutrino magnetic moment ana. I helped (re)produce the systematic samples for the nueccmec enhanced sample. Technically I also investigated the nominal ND sample and whether it would be better to use the decaf sample, but this led nowhere... Technically I also analysed the electron recoil energy and angle resolution and decided on the binning (although not finished and talked about here). I did the systematics study and implemented the systematic shifts for the detector systematics for numm. I implemented the fitting framework for the neutrino magnetic moment analysis for both the template fit (not used here) and the counting experiment. I did the actual fit and got the final results.

# CHAPTER 1

## In this analysis, I aim to detect a potential signal of the effective muon neutrino **Measuring the Muon Neutrino Magnetic Moment**

magnetic moment in the [NOvA](#) Near Detector (ND). This signal would manifest as an excess of neutrino-on-electron ( $\nu$ -on-e) elastic scattering interactions at low electron recoil energies, proportional to the value of the effective neutrino magnetic moment, over the Standard Model (SM) background. If no significant excess is observed, I will establish an upper limit on the effective muon neutrino magnetic moment.

Detecting the neutrino magnetic moment ( $\mu_\nu$ ) would provide definitive evidence of new Beyond Standard Model (BSM) physics, and measuring its value would help identify the appropriate [BSM](#) theory. As current and planned experiments can only detect an anomalously large neutrino magnetic moment, observing such a signature would strongly suggest that neutrinos are Majorana particles and would have significant implications for astrophysics and cosmology [1].

The best model-independent experimental results on the neutrino magnetic moment come from experiments searching for dark matter using xenon-based detectors. These highly sensitive detectors detect solar neutrinos, which are part of the background in dark matter searches but can be reanalyzed for other purposes. In 2020, the XENON1T experiment observed [2] a low energy excess of solar neutrinos, which could correspond to a signal from an anomalously large effective magnetic moment within  $\mu_{\nu_\odot} \in (0.14, 0.29) \times 10^{-10} \mu_B$  at 90 % Confidence Level (C.L.), where  $\nu_\odot$  marks solar neutrinos. However, this result was disfavoured by the follow-up XENONnT experiment in 2022 [3], which saw no excess and set the current world-leading limit on neutrino magnetic moment at  $\mu_{\nu_\odot} < 0.063 \times 10^{-10} \mu_B$  at 90 % C.L.. Other solar neutrino experiments also reported null results regarding neutrino magnetic moment [4, 5], placing less stringent limits on its value. Given some basic assumptions [5, 6] this limit for solar neutrinos would correspond to a limit on muon neutrino effective magnetic moment of  $\mu_{\nu_\mu} < 0.137 \times 10^{-10} \mu_B$ . However, the relationship between ef-

fective magnetic moments of different neutrino flavours may be non-trivial, especially in the context of possible new [BSM](#) physics, and studying muon neutrinos remains an important endeavour [7].

The best results for  $\nu_\mu$  and  $\bar{\nu}_\mu$  come from accelerator-based stopped pion neutrino sources [8, 9], which also do not observe any low energy excess and provide an upper limit on the effective muon neutrino magnetic moment of  $\mu_{\nu_\mu} < 6.8 \times 10^{-10} \mu_B$  at 90 % C.L. [8]. Stopped pion neutrino sources provide well-understood beams made up of  $\nu_\mu$ ,  $\bar{\nu}_\mu$  and  $\nu_e$  with energies up to 52.8 MeV. Slightly looser limits come from pion decay-in-flight accelerator-based measurements (similar to [NOvA](#)) [10, 11], which provide a limit of  $\mu_{\nu_\mu} < 8.5 \times 10^{-10} \mu_B$  at 90 % C.L..

Thanks to the very intense and highly pure beam of muon neutrinos and antineutrinos, and a detector designed for the reconstruction and identification of events with electrons in the final state, [NOvA](#) is well-positioned to provide a highly competitive, and possibly even world-leading, measurement (or limit) of the effective muon neutrino magnetic moment. A previous analysis of [NOvA ND](#) data for a measurement of the effective muon neutrino magnetic moment was presented in a thesis [12], providing a (statistics-only) limit of  $\mu_{\nu_\mu} < 15.8 \times 10^{-10} \mu_B$  at 90 % C.L..

Additionally,  $\nu$ -on-e elastic scattering interactions are used in various other analyses in [NOvA](#), specifically in efforts to constrain the neutrino beam prediction [13, 14] and in the search for Light Dark Matter (LDM) [15]. These analyses developed various tools and methods that can be utilized in the search for a neutrino magnetic moment.

In this chapter, I will provide an overview of the theory of neutrino electromagnetic interactions in Sec. 1.1, focusing on the effective neutrino magnetic moment and its implications for  $\nu$ -on-e measurements and other theoretical considerations. In Sec. 1.2, I will discuss the analysis strategy, the signal and background definition, as well as the data and simulation samples and the analysis weights. Following this, in Sec. 1.3 I will explain the selection of events for this analysis, while in Sec. 1.4 I will address the relevant systematic uncertainties. I will present the results of this analysis in Sec. 1.5 and discuss their implications in Sec. 1.6. Finally, section 1.7 will summarise the findings of this analysis.

## 1.1 Theory of the Neutrino Magnetic Moment

As was described in Sec. ??, neutrinos in the SM are massless and electrically neutral particles. However, even SM neutrinos can have electromagnetic interaction through loop diagrams involving charged leptons and the W boson, covered by the neutrino charge radius [1].

In general BSM theories, considering interactions with a single photon as shown on Fig. 1.1, neutrino electromagnetic interactions can be described by an effective interaction Hamiltonian [16]

$$\mathcal{H}_{em}^{(\nu)}(x) = \sum_{k,j=1}^N \bar{\nu}_k(x) \Lambda_{\mu}^{kj} \nu_j(x) A^{\mu}(x). \quad (1.1)$$

Here  $\nu_k(x)$ ,  $k = 1, \dots, N$ , are neutrino fields in the mass basis with  $N$  neutrino mass states,  $\Lambda_{\mu}^{kj}$  is a general vertex function and  $A^{\mu}(x)$  is the electromagnetic field.

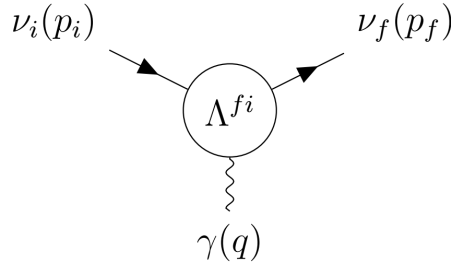


Figure 1.1: Effective coupling of neutrinos with one photon electromagnetic field.

The vertex function  $\Lambda_{\mu}^{fi}(q)$  is generally a matrix and, in the most general case consistent with the SM gauge invariance [17, 18], can be written in terms of linearly independent products of Dirac matrices ( $\gamma$ ) and only depends on the four momentum of the photon ( $q = p_f - p_i$ ):

$$\begin{aligned} \Lambda_{\mu}^{fi}(q) = & \mathbb{F}_1^{fi}(q^2) q_{\mu} + \mathbb{F}_2^{fi}(q^2) q_{\mu} \gamma_5 + \mathbb{F}_3^{fi}(q^2) \gamma_{\mu} + \mathbb{F}_4^{fi}(q^2) \gamma_{\mu} \gamma_5 + \\ & \mathbb{F}_5^{fi}(q^2) \sigma_{\mu\nu} q^{\nu} + \mathbb{F}_6^{fi}(q^2) \epsilon_{\mu\nu\rho\gamma} q^{\nu} \sigma^{\rho\gamma}, \end{aligned} \quad (1.2)$$

where  $\mathbb{F}_i^{fi}(q^2)$  are six Lorentz invariant form factors and  $\delta$  and  $\epsilon$  are the Dirac delta and the Levi-Civita symbols respectively.

Applying conditions of hermiticity ( $\mathcal{H}_{em}^{(\nu)\dagger} = \mathcal{H}_{em}^{(\nu)}$ ) and of the gauge invariance

of the electromagnetic field, the vertex function can be rewritten as

$$\Lambda_\mu^{fi}(q) = (\gamma_\mu - q_\mu \not{q}/q^2) \left[ \mathbb{F}_Q^{fi}(q^2) + \mathbb{F}_A^{fi}(q^2) q^2 \gamma_5 \right] - i\sigma_{\mu\nu} q^\nu \left[ \mathbb{F}_M^{fi}(q^2) + i\mathbb{F}_E^{fi}(q^2) \gamma_5 \right], \quad (1.3)$$

where  $\mathbb{F}_Q^{fi}$ ,  $\mathbb{F}_M^{fi}$ ,  $\mathbb{F}_E^{fi}$  and  $\mathbb{F}_A^{fi}$  are hermitian matrices representing the charge, dipole magnetic, dipole electric and anapole neutrino form factors respectively. It is clear that the vertex function only depends on the square of the four momentum of the photon  $q^2$ . In coupling with a real photon ( $q^2 = 0$ ) these form factors become the neutrino charge and magnetic, electric and anapole moments respectively. Additionally, the neutrino charge radius corresponds to the second term in the expansion of the charge form factor [16].

The above expression can be simplified [19] as

$$\Lambda_\mu^{fi}(q) = \gamma_\mu \left( Q_{\nu_{fi}} + \frac{q^2}{6} \langle r^2 \rangle_{\nu_{fi}} \right) - i\sigma_{\mu\nu} q^\nu \mu_{\nu_{fi}}, \quad (1.4)$$

where  $Q_{\nu_{fi}}$ ,  $\langle r^2 \rangle_{\nu_{fi}}$ , and  $\mu_{\nu_{fi}}$  are the neutrino charge, effective charge radius (also containing anapole moment), and an effective magnetic moment (also containing electric moment) respectively. This is possible thanks to the similar effects of the neutrino charge radius and the anapole moment, and of the neutrino magnetic and electric moments, on neutrino interactions. Therefore, these are the three neutrino electromagnetic properties (charge, effective charge radius and effective magnetic moment) measured in experiments.

The neutrino electric charge is primarily constrained through measurements of the neutrality of matter and through cosmological observations, which provide much better constraints than neutrino oscillation experiments [16]. On the other hand, the neutrino charge radius would manifest as an increase in the size of the  $\nu$ -on- $e$  elastic scattering coupling constants, allowing it to be studied in neutrino oscillation experiments such as NOvA. Additionally, the value of the neutrino charge radius in the SM is only an order of magnitude smaller than the current world-leading limits [20] and measuring it could either confirm the validity of neutrino interactions in the SM, or open possibilities to non-standard contributions to neutrino scattering [16]. However, measurement of the neutrino charge radius is not part of this analysis, but may be included in the future re-analysis of the  $\nu$ -on- $e$  interactions in the NOvA ND.

### 1.1.1 Neutrino Electric and Magnetic Dipole Moments

The size and effect of neutrino electromagnetic properties depend on the specific [BSM](#) theory applied. Evaluating one loop diagrams in the minimally extended [SM](#) with three right-handed Dirac neutrinos, as described in Sec. ??, gives the first approximation of the electric and magnetic moments, which are now  $3 \times 3$  matrices with elements:

$$\left. \begin{array}{l} \mu_{kj}^D \\ i\epsilon_{kj}^D \end{array} \right\} \simeq \frac{3eG_F}{16\sqrt{2}\pi^2} (m_k \pm m_j) \left( \delta_{kj} - \frac{1}{2} \sum_{l=e,\mu,\tau} U_{lk}^* U_{lj} \frac{m_l^2}{m_W^2} \right), \quad (1.5)$$

where  $m_k, m_j$  are the neutrino masses and  $m_l$  are the masses of charged leptons which appear in the loop diagrams [16]. The  $D$  superscript denotes Dirac neutrinos and  $M$  denotes Majorana neutrinos throughout this section. Also,  $e$  is the electron charge,  $G_F$  is the Fermi coupling constant,  $U$  is the Pontecorvo-Maki-Nakagawa-Sakata (PMNS) neutrino oscillation matrix, and  $m_W$  is the mass of the  $W$  boson. Higher order electromagnetic corrections were neglected, but can also have a significant contribution, depending on the theory.

It can be seen that Dirac neutrinos have no diagonal electric moments ( $\epsilon_{kk}^D = 0$ ) and their diagonal magnetic moments are approximately

$$\mu_{kk}^D \simeq \frac{3eG_F m_k}{8\sqrt{2}\pi^2} \simeq 3.2 \times 10^{-19} \left( \frac{m_k}{\text{eV}} \right) \mu_B, \quad (1.6)$$

where  $\mu_B$  is the Bohr magneton which represents the value of the electron magnetic moment [16]. Neutrino magnetic moments are therefore strongly suppressed by the smallness of neutrino masses, with theoretical predictions in Eq. 1.6 several orders of magnitude below the reach of current experiments [19].

The transition magnetic moments in the minimally extended [SM](#) from Eq. 1.5 are suppressed with respect to the largest of the diagonal magnetic moments by at least a factor of  $10^{-4}$  due to the  $m_W^2$  in the denominator. The transition electric moments are even smaller due to the mass difference in Eq. 1.5. Therefore an experimental observation of a magnetic moment larger than in Eq. 1.6 would indicate physics beyond the minimally extended [SM](#) [16, 21].

The suppression of the neutrino magnetic moment by the smallness of its mass



can be also expressed in a general case [21]. The ‘natural’ upper limits on the size of the neutrino magnetic moment for any BSM theory that has New Physics (NP) generated at a scale  $\Lambda_{NP}$  can be expressed as [22]

$$\mu_\nu^D (\mu_B) \lesssim 3 \times 10^{-15} \frac{m_\nu^D (\text{eV})}{[\Lambda_{NP} (\text{TeV})]^2}. \quad (1.7)$$

Therefore for  $\Lambda_{NP} \simeq 1\text{TeV}$  and  $m_\nu^D \lesssim 1\text{eV}$  the limit becomes  $\mu_\nu^D \lesssim 3 \times 10^{-15} \mu_B$ , well below the current experimental capabilities. However, these upper bounds only apply if NP is generated well above the electroweak scale  $\Lambda_{EW} \sim 100\text{ GeV}$  [16].

For Majorana neutrinos, the magnetic and electric form factors (and therefore the magnetic and electric moment matrices) are antisymmetric, thus Majorana neutrinos only have transition moments. The simplest extension of the SM that includes Majorana neutrinos requires either the addition of a Higgs triplet, or right-handed neutrinos together with a Higgs singlet [16]. Neglecting the Feynman diagrams which depend on the model of the scalar sector, the magnetic and electric dipole moments are

$$\left. \begin{matrix} \mu_{kj}^M \\ \epsilon_{kj}^D \end{matrix} \right\} \simeq \mp \frac{3ieG_F}{16\sqrt{2}\pi^2} (m_k \pm m_j) \sum_{l=e,\mu,\tau} \text{Im/Re} [U_{lk}^* U_{lj}] \frac{m_l^2}{m_W^2}, \quad (1.8)$$

where Im is for  $\mu_{kj}^M$  and Re is for  $\epsilon_{kj}^D$ . These are difficult to compare to the Dirac case, due to possible presence of Majorana phases in the PMNS matrices, but it is clear that they have the same order of magnitude as Dirac transition dipole moments. However, the neglected model dependent contributions can enhance the transition dipole moments for Majorana neutrinos [16].

The natural upper bound on the Majorana magnetic moment is less strict compared to the Dirac neutrinos, due to the antisymmetric nature of Majorana magnetic moment, which requires additional Yukawa couplings in the BSM theory compared to Dirac neutrinos, which can enhance the maximal possible magnetic moment [21]. The limit for Majorana neutrinos can be expressed as

$$\mu_{\alpha\beta}^M (\mu_B) \leq 4 \times 10^{-9} \frac{[m_\nu^M]_{\alpha\beta} (\text{eV})}{[\Lambda_{NP} (\text{TeV})]^2} \frac{m_\tau^2}{|m_\alpha^2 - m_\beta^2|}, \quad \alpha, \beta \in \{e, \mu, \tau\}. \quad (1.9)$$

Here, the neutrino magnetic moment is expressed in the flavour basis instead of the mass basis, since the charged lepton masses are diagonal here. The two bases are

related by

$$\mu_{ij} = \sum_{\alpha\beta} \mu_{\alpha\beta} U_{\alpha i}^* U_{\beta j}. \quad (1.10)$$

and the effect of the neutrino magnetic moment on neutrino interactions does not depend on the choice of the basis[23].

These considerations imply, that if a magnetic moment  $\mu \gtrsim 10^{-15} \mu_B$  were measured, neutrinos are almost certainly Majorana particles [21].

### Effective neutrino magnetic moment

As mentioned above, the neutrino magnetic moment measured in experiments is the so-called effective neutrino magnetic moment, which is a combination of electric and magnetic dipole moments and depends on the neutrino source and oscillations. In the ultra-relativistic limit, the effective neutrino magnetic moment is

$$\mu_{\nu_l}^2(L, E_\nu) = \sum_j \left| \sum_k U_{lk}^* e^{\mp i \Delta m_{kj}^2 L / 2E_\nu} (\mu_{jk} - i \epsilon_{jk}) \right|^2, \quad (1.11)$$

where the minus sign in the exponent is for neutrinos and the plus sign for antineutrinos [16]. Therefore, the only difference between the effective neutrino and antineutrino magnetic moment is in the phase induced by neutrino oscillations. For experiments with baselines short enough that neutrino oscillations would not have time to develop ( $\Delta m^2 L / 2E_\nu \ll \sim 1$ ), such as the [NOvA ND](#), the effective magnetic moment is the same for neutrinos and antineutrinos and is independent of the neutrino energy.

Since the effective magnetic moment depends on the initial neutrino flavour, it is different for experiments studying neutrinos from different sources. Additionally, experiments such as solar neutrino experiments, need to include matter effects on the neutrino oscillations. Therefore the reports on the value (or upper limit) of the effective neutrino magnetic moment are not directly comparable between different types of neutrino experiments.

### 1.1.2 Measuring the Neutrino Magnetic Moment

The most sensitive method to measure the neutrino magnetic moment is the low energy elastic scattering of (anti)neutrinos on electrons [16]. The schematic diagram for this interaction is shown in Fig. 1.2, where the recoil electron's kinetic energy is defined as ( $T_e = E_{e'} - m_e$ ) and the recoil angle with respect to the incoming neutrino beam ( $\theta$ ) is shown.

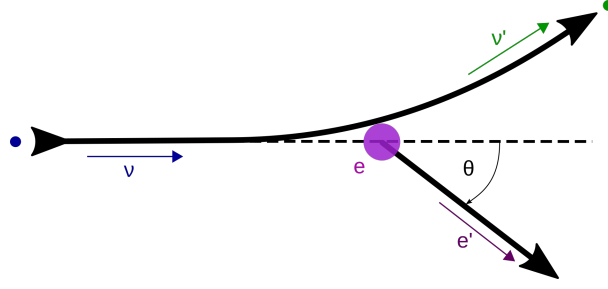


Figure 1.2: Neutrino-on-electron elastic scattering diagram

Since the  $\nu$ -on- $e$  interaction is governed by simple  $2 \rightarrow 2$  kinematics, it can be shown that

$$(P_\nu - P_{e'})^2 = (P_{\nu'} - P_e)^2, \quad (1.12)$$

$$m_\nu^2 + m_e^2 - 2E_\nu E_{e'} + 2E_\nu p_{e'} \cos \theta = m_{\nu'}^2 + m_e^2 - 2E_{\nu'} m_e. \quad (1.13)$$

From the energy conservation

$$E_\nu + m_e = E_{\nu'} + E_{e'} = E_{\nu'} + T_e + m_e \Rightarrow E_{\nu'} = E_\nu - T_e \quad (1.14)$$

it follows that

$$E_\nu p_{e'} \cos \theta = E_\nu E_{e'} - E_{\nu'} m_e = E_\nu (T_e + m_e) - (E_\nu - T_e) m_e = T_e (E_\nu + m_e), \quad (1.15)$$

$$\cos \theta = \frac{E_\nu + m_e}{E_\nu} \sqrt{\frac{T_e^2}{E_{e'}^2 - m_e^2}} = \frac{E_\nu + m_e}{E_\nu} \sqrt{\frac{T_e^2}{T_e^2 + 2T_e m_e}}. \quad (1.16)$$

And finally

$$\cos \theta = \frac{E_\nu + m_e}{E_\nu} \sqrt{\frac{T_e}{T_e + 2m_e}}. \quad (1.17)$$

Which can be rearranged to get

$$T_e = \frac{2m_e E_\nu^2 \cos^2 \theta}{(E_\nu + m_e)^2 - E_\nu^2 \cos^2 \theta}. \quad (1.18)$$

The electron's kinetic energy is therefore constrained as

$$T_e \leq \frac{2E_\nu^2}{2E_\nu + m_e}, \quad (1.19)$$

which corresponds to the limit  $\cos \theta \rightarrow 1$  when the recoil electron goes exactly forward in the incident neutrino direction, as depicted in Fig. 1.3.

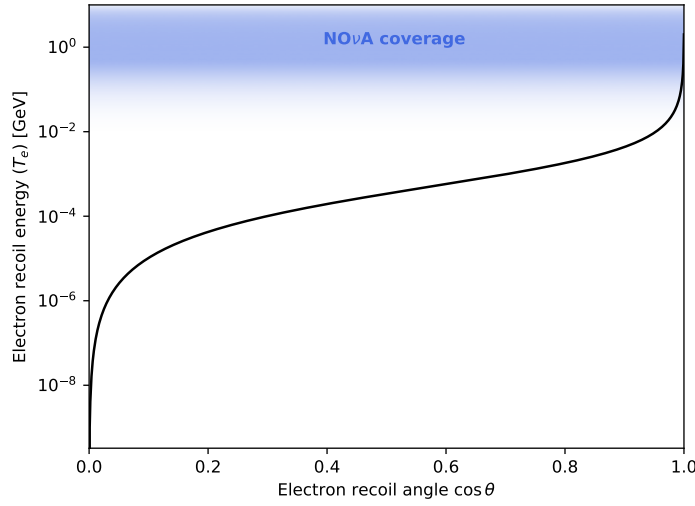


Figure 1.3: Relation between the recoil electron's kinetic energy and angle for the  $\nu$ -on-e elastic scattering. The coverage of the **NOvA** detectors for measuring the electron recoil energy is shown in blue. Only very forward electrons are therefore recorded in **NOvA**.

Considering  $E_\nu \sim \text{GeV}$ , it is useful to approximate  $\frac{m_e^2}{E_\nu^2} \rightarrow 0$ . Additionally, considering only very small electron recoil angles, meaning  $\theta^2 \cong (1 - \cos^2 \theta)$ , applied to Eq. 1.17 results in

$$T_e \theta^2 \cong T_e \left( 1 - \left( \frac{E_\nu + m_e}{E_\nu} \right)^2 \frac{T_e}{T_e + 2m_e} \right) = T_e \left( 1 - \left( 1 + \frac{2m_e}{E_\nu} \right) \frac{T_e}{T_e + 2m_e} \right), \quad (1.20)$$

therefore

$$T_e \theta^2 \cong \frac{2m_e T_e}{T_e + 2m_e} \left( 1 - \frac{T_e}{E_\nu} \right) = 2m_e \left( \frac{1}{1 + \frac{2m_e}{T_e}} \right) \left( 1 - \frac{T_e}{E_\nu} \right), \quad (1.21)$$

and finally

$$T_e \theta^2 \cong 2m_e \left(1 - \frac{T_e}{E_\nu}\right) < 2m_e. \quad (1.22)$$

This is a strong limit that very clearly distinguishes the  $\nu$ -on-e elastic scattering events from other similar interactions involving single electron (mainly the  $\nu_e$  Charged Current (CC) interactions).

### Neutrino Magnetic Moment Cross Section

In the ultra-relativistic limit, the neutrino magnetic moment interaction flips the neutrino helicity, while the SM weak interaction conserves it, which means it is possible to add the two contributions to the total  $\nu$ -on-e cross section incoherently (without interference terms) [16]:

$$\frac{d\sigma_{\nu\text{-on-e}}}{dT_e} = \left(\frac{d\sigma_{\nu\text{-on-e}}}{dT_e}\right)_{\text{SM}} + \left(\frac{d\sigma_{\nu\text{-on-e}}}{dT_e}\right)_{\text{MAG}}. \quad (1.23)$$

The SM contribution can be expressed as [16, 24]:

$$\left(\frac{d\sigma_{\nu\text{-on-e}}}{dT_e}\right)_{\text{SM}} = \frac{2G_F^2 m_e}{\pi} \left\{ g_1^2 + g_2^2 \left(1 - \frac{T_e}{E_\nu}\right)^2 - g_1 g_2 \frac{m_e T_e}{E_\nu^2} \right\}, \quad (1.24)$$

where the coupling constants  $g_1$  and  $g_2$  differ between neutrino flavours and between neutrinos and antineutrinos. Their values are:

$$g_1^{\nu_e} = g_2^{\bar{\nu}_e} = \sin^2 \theta_W + 1/2, \quad g_2^{\nu_e} = g_1^{\bar{\nu}_e} = \sin^2 \theta_W, \quad (1.25)$$

$$g_1^{\nu_{\mu,\tau}} = g_2^{\bar{\nu}_{\mu,\tau}} = \sin^2 \theta_W - 1/2, \quad g_2^{\nu_{\mu,\tau}} = g_1^{\bar{\nu}_{\mu,\tau}} = \sin^2 \theta_W, \quad (1.26)$$

where  $\sin^2 \theta_W \cong 0.23$ .

The total SM cross section, and therefore the number of SM  $\nu$ -on-e interactions, depends on the neutrino energy and the minimum measured electron recoil energy. However, in general the cross section for  $\nu_e$  is about 2.5 times larger than for the  $\bar{\nu}_e$ , about 6 times larger than for  $\nu_{\mu/\tau}$  and about 7 times larger than for  $\bar{\nu}_{\mu/\tau}$ .

The neutrino magnetic moment contribution is [16, 25]:

$$\left(\frac{d\sigma_{\nu\text{-on-e}}}{dT_e}\right)_{\text{MAG}} = \frac{\pi \alpha^2}{m_e^2} \left(\frac{1}{T_e} - \frac{1}{E_\nu}\right) \left(\frac{\mu_{\nu_l}}{\mu_B}\right)^2, \quad (1.27)$$

where  $\alpha$  is the fine structure constant and  $\mu_{\nu_l}$  is the effective magnetic moment of  $\nu_l$ . The total cross section now only depends on the neutrino energy and on the effective magnetic moment, but is the same for neutrinos and antineutrinos.

The comparison of the SM and the neutrino magnetic moment differential cross sections is shown in Fig.1.4. Whereas the SM cross section is approximately uniform for  $T_e \rightarrow 0$ , the neutrino magnetic moment cross section rises to infinity. However, this reach is limited by the experimental capabilities of detecting electrons with very low energies. The (possible) NOvA coverage is shown with a shaded blue region, with current capability reaching  $T_e = 0.5$  GeV. Future analyses might extend this reach to lower  $T_e$ , with the lowest possible detectable electron recoil energy  $T_{e,min} \approx 0.01$  GeV, as discussed in Sec. ??.

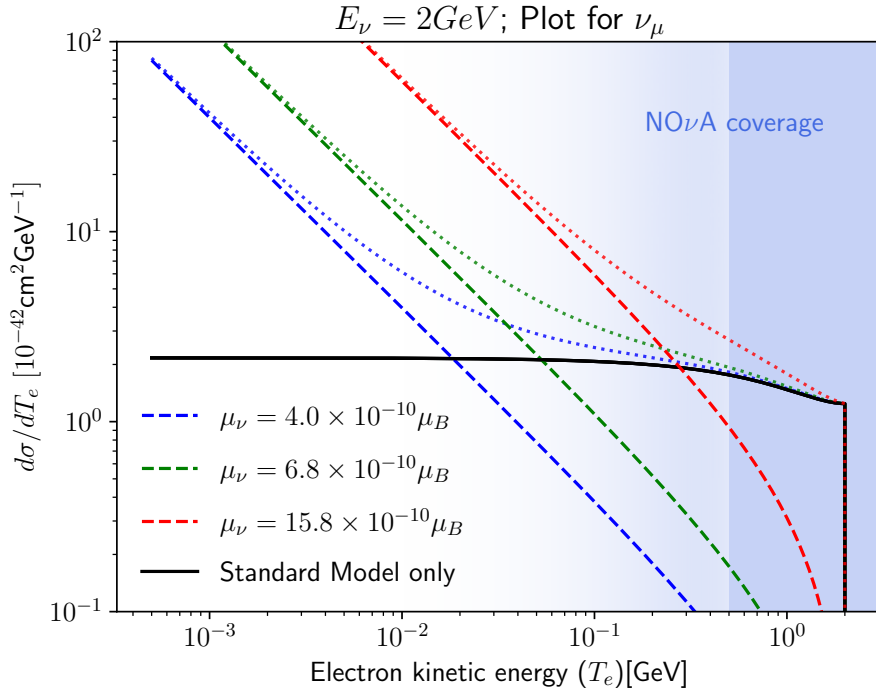


Figure 1.4: Comparison of the neutrino magnetic moment (coloured) and the SM (black) cross sections for the  $\nu$ -on- $e$  elastic scattering. Different colours depict different values of the neutrino magnetic moment, with red corresponding to the previous NOvA measurement, green the LSND result, and blue a possible ultimate NOvA sensitivity, as discussed in the introduction to this chapter. Dashed lines are the individual cross sections and dotted lines are the added total cross section with the standard model contribution. NOvA coverage of electron recoil energies is shown in shaded blue.

Calculating the ratio of the neutrino magnetic moment and the SM cross sections, as shown in Fig. 1.5, can serve as a proxy to estimate the number of neutrino magnetic

moment events in relation to the predicted number of **SM** events, if the  $E_\nu$  and  $T_e$  are known. Additionally, comparing the ratio of the total cross sections can reveal the expected total number of neutrino magnetic moment events as a function of the predicted number of **SM** events. Considering  $E_\nu = 2 \text{ GeV}$ ,  $\mu_\nu = 6.8 \times 10^{-10} \mu_B$  (current best limit for  $\nu_\mu$  from LSND), and integrating differential cross sections for  $\nu_\mu$  in Eq. 1.24 and 1.27 from  $T_{e,min}$  to  $T_{e,max} \rightarrow 2 \text{ GeV}$  results in

$$\frac{\sigma_{\text{MAG}}}{\sigma_{\text{SM}}} \approx \begin{cases} 0.035 & T_{e,min} = 0.5 \text{ GeV}, \\ 0.14 & T_{e,min} = 0.01 \text{ GeV}. \end{cases} \quad (1.28)$$

Therefore, at the current **NOvA** detection capabilities, there are about 0.035 times as many neutrino magnetic moment  $\nu$ -on-e events than **SM** ones. This can be compared with the expected statistical uncertainty on the **SM** background, which in the case of Poisson distributed events is the square root of the number of predicted events. Consequently, it is possible to assess the minimal number of **SM**  $\nu$ -on-e events necessary for the magnetic moment signal to be detected above the **SM** background (without considering systematic uncertainties) as

$$N_{\text{SM}} > 1/0.035^2 \approx 816. \quad (1.29)$$

However, this approximation is calculated only for one value of  $E_\nu$ , but can be used to assess the sensitivity of the experiment.

As can be seen in Fig. 1.4 and Fig. 1.5, the magnetic moment contribution exceeds the **SM** contribution for low enough  $T_e$ . This can be approximated as [16]:

$$T_e \lesssim \frac{\pi^2 \alpha^2}{G_F^2 m_e^3} \left( \frac{\mu_\nu}{\mu_B} \right)^2 \simeq 2.9 \times 10^{19} \left( \frac{\mu_\nu}{\mu_B} \right)^2 [\text{MeV}], \quad (1.30)$$

which does not depend on the neutrino energy. Therefore, experiments sensitive to lower energetic electrons are significantly more sensitive to the neutrino magnetic moment.

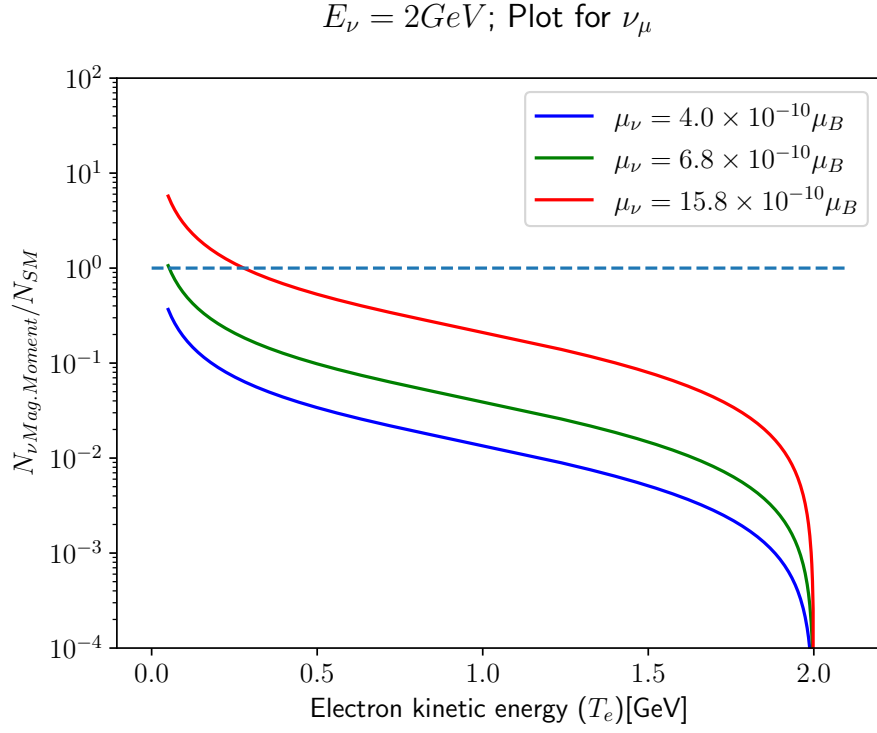


Figure 1.5: Ratio of the neutrino magnetic moment cross section to the [SM](#) cross section for the  $\nu$ -on- $e$  elastic scattering of 2 GeV  $\nu_\mu$ . Different colours depict different effective muon neutrino magnetic moment values, with red corresponding to the previous [NOvA](#) measurement, green the LSND result, and blue a possible ultimate [NOvA](#) sensitivity, as discussed in the introduction to this chapter.



## 1.2 Analysis Overview

Our analysis strategy for measuring the effective muon neutrino magnetic moment in the **NOvA ND** is based on comparing the total number of reconstructed and selected events in data with the prediction. The predicted events consist of the signal, which depends on the size of the effective muon neutrino magnetic moment, and of the background, which corresponds to the **SM-only** (null) hypothesis without any neutrino magnetic moment. We define the signal as true  **$\nu$ -on-e** elastic scattering interactions, created with the use of the neutrino magnetic moment cross section instead of the **SM** cross section, as described in Sec. 1.1.2. Additionally, the signal events are required to have their true interaction vertex contained within the **ND** to exclude events originating from outside of the detector.

The data used in this analysis were collected from the start of **NOvA ND** data taking on the August 22<sup>nd</sup>, 2014, until February 3<sup>rd</sup>, 2021. This is the **ND** data that were used in the latest **NOvA** neutrino oscillations result [26], with an additional year. Although more data have been collected since February 2021, they are still being processed and are not available at the time of writing this thesis. The total exposure of the data sample is approximately  $13.8 \times 10^{20}$  Protons On Target (POT). This exposure is used throughout this chapter to scale the predicted distributions and number of events.

This analysis uses the standard **NOvA** simulation and reconstruction tools, as were discussed in Sec. ?? and ?. The simulation was created with approximately four times larger statistics than the data to limit statistical uncertainties from simulation. The total exposure for the simulation is approximately  $55.4 \times 10^{20}$  **POT**. For the systematic uncertainty studies only a portion of this full sample is used, specifically  $19.3 \times 10^{20}$  **POT**.

Corrections for known limitations in the simulation are applied in the form of analysis weights applied to each event based on how it is affected by specific variations in the simulation. This includes the corrections for the neutrino beam prediction based on the external measurements used by the Package to Predict the Flux (PPFX) (Sec. ??), and, for the non- **$\nu$ -on-e** background only, also the internal and external measurements that constrain the neutrino interaction prediction inside GENIE.

The cross section corrections are not applied to the  **$\nu$ -on-e** events, as they are as-

sumed to be known precisely from theory. However, the GENIE Monte Carlo (MC) simulation only considers tree-level **SM  $\nu$ -on-e** interactions [13], as described in Sec. 1.1.2, and doesn't account for any higher order terms, which are described by radiative corrections. Radiative corrections can be expressed by two adjustments to the tree-level **SM  $\nu$ -on-e** cross section [27]. First, the values of the weak coupling constants are changed as [28]

$$g_1^{\nu_e} \rightarrow 0.7276, \quad g_1^{\nu_\mu} \rightarrow -0.2730, \quad g_2 \rightarrow 0.2334. \quad (1.31)$$

Second, there are additional terms added to the cross section equation. Considering only one-loop corrections, the full  **$\nu$ -on-e** cross section can be expressed as<sup>1</sup> [29]

$$\left( \frac{d\sigma_{\nu\text{-on-e}}}{dy} \right)_{\text{Rad. Corr.}} = \frac{G_F^2 s}{\pi} \left\{ g_1^2 \left( 1 + \frac{\alpha}{\pi} X_1 \right) + g_2^2 (1-y)^2 \left( 1 + \frac{\alpha}{\pi} X_2 \right) - g_1 g_2 \frac{m_e y}{E_\nu} \right\}, \quad (1.32)$$

where

$$y = \frac{T_e + E_\gamma}{E_\nu}, \quad (1.33)$$

$s = 2E_\nu m_e + m_e^2$  is the Mandelstam variable,

$$X_1 = -\frac{2}{3} \log \left( \frac{2yE_\nu}{m_e} \right) + \frac{y^2}{24} - \frac{5y}{12} - \frac{\pi^2}{6} + \frac{23}{72} \quad (1.34)$$

and

$$X_2 = -\frac{2}{3} (1-y)^2 \log \left( \frac{2yE_\nu}{m_e} \right) - \frac{y^2}{18} - \frac{\pi^2}{6} (1-y)^2 - \frac{2y}{9} + \frac{23}{72}. \quad (1.35)$$

In practice, radiative corrections can be implemented as a weight, where each true  **$\nu$ -on-e** event is weighted by a ratio

$$\text{weight}_{\text{Rad. Corr.}}(E_\nu, T_e) = \left( \frac{d\sigma_{\nu\text{-on-e}}}{dy} \right)_{\text{Rad. Corr.}} \bigg/ \left( \frac{d\sigma_{\nu\text{-on-e}}}{dy} \right)_{\text{GENIE 3}}; \quad (1.36)$$

Analogically to the radiative correction weight, it is possible to create a neutrino magnetic moment weight as a ratio between the neutrino magnetic moment and the **SM** differential cross sections for the  **$\nu$ -on-e** interactions. This can then serve to pre-

---

<sup>1</sup>There is technically a third correction term  $X_3$  by the  $g_1 g_2$  term, which is however negligible for  $E_\nu \sim \text{GeV}$ .

dict the number of  $\nu$ -on-e events created by the neutrino magnetic moment interaction (which make up the signal), without the need for an additional simulation. This is possible thanks to the theoretically very well understood properties of the  $\nu$ -on-e interaction, as described in Sec. 1.1.2. Therefore, the signal sample is created from the true  $\nu$ -on-e sample, with the magnetic moment weight applied. The weight has a form:

$$\text{weight}_{\nu\text{Mag. Mom.}}(E_\nu, T_e) = \left( \frac{d\sigma_{\nu\text{-on-e}}}{dy} \right)_{\nu\text{Mag. Mom.}} \bigg/ \left( \frac{d\sigma_{\nu\text{-on-e}}}{dy} \right)_{\text{GENIE 3}}, \quad (1.37)$$

where

$$\left( \frac{d\sigma_{\nu\text{-on-e}}}{dy} \right)_{\nu\text{Mag. Mom.}} = E_\nu \left( \frac{d\sigma_{\nu\text{-on-e}}}{dT_e} \right)_{\nu\text{Mag. Mom.}}. \quad (1.38)$$

Due to the relatively low cross section of the  $\nu$ -on-e interaction, the nominal simulation sample contains very few  $\nu$ -on-e events, which could result in a significant statistical uncertainty from simulation. To avoid this, we created a  $\nu$ -on-e-enhanced simulation sample, which is mainly made up of  $\nu$ -on-e events with a total exposure of  $1.72 \times 10^{24}$  POT. There are a few non- $\nu$ -on-e background events overlaid on top of the  $\nu$ -on-e events to properly account for the possible reconstruction effects of the pileup of neutrino interactions in a single spill [13], since in the real detector, the hits from the true  $\nu$ -on-e interaction can be clustered together into another interaction, or additional hits can be clustered together into the  $\nu$ -on-e event. To save up on unnecessary disk space and processing usage, the enhanced  $\nu$ -on-e sample does not include any cross section related parameters and variables, as the  $\nu$ -on-e interaction is assumed to be known exactly from theory. Therefore, we do not apply cross section weights or account for cross section systematic uncertainties for  $\nu$ -on-e events.

The cross section tuning procedure in NOvA (Sec. ??) applies large weights to Meson Exchange Current (MEC) events in some parts of the parameter space. However, after the full event selection (Sec. 1.3) only a small number of MEC events remain in the detector. This was shown to be an issue especially for the  $\nu_e$ CC MEC events [13]. Applying large tuning corrections to a small number of events results in large statistical fluctuations. To avoid this, we created another special sample with enhanced number of  $\nu_e$ CC MEC events, following the same procedure as for the  $\nu$ -on-e-enhanced sample, with an exposure of  $1.99 \times 10^{24}$  POT.

A summary of the simulation samples and analysis weights for the four different types of signal and background components is shown in Tab. 1.1. In the following chapter, the  $\nu_e$ CC MEC background is added into the ‘Other background’ sample, even though it is created from a separate simulation.

Table 1.1: Overview of the simulation samples and analysis weight used for the different signal and background components.

Signal type	Sample	Weight
Signal	Enhanced $\nu$ -on-e	Flux & $\nu$ Mag. Moment
$\nu$ -on-e background	Enhanced $\nu$ -on-e	Flux & Rad. Corr.
$\nu_e$ CC MEC background	Enhanced $\nu_e$ CC MEC	Flux & Cross Sec.
Other background	Nominal ND	Flux & Cross Sec.

### 1.3 Event Selection

We are searching for  $\nu$ -on-e elastic scattering events, characterised by a single very forward going electron shower, specifically focusing on low electron recoil energies. The main backgrounds for our analysis come from  $\nu_e$ CC interactions, which produce an electron with additional activity, and interactions that produce  $\pi^0$ , which decays into two photons producing electromagnetic showers, where each can look similar to the  $\nu$ -on-e signal. Additionally, there are  $\nu_\mu$ CC interactions, which are generally easy to distinguish from our signal, however, their very high abundance in the NOvA ND makes them a dominant background nevertheless.

I explain the motivation behind each cut of the event selection and discuss their effect on the neutrino magnetic moment events below. I also consider possible improvements to the event selection for a future (re-)analysis.

The strategy for event selection is as follows. First, I remove events that failed reconstruction or data collection, described in Sec. 1.3.1 and 1.3.2. Then, I apply pre-selection cuts that remove obvious background (Sec. 1.3.3), while limiting the reduction of the signal efficiency to about 0.25 %. Following this, I apply the containment cuts (Sec. 1.3.4) that remove events that are either not fully contained within the detector, or events that originate from outside of the detector, such as rock muons. Afterwards, I perform a cut-based Multi Variate Analysis (MVA) on a selection of vari-

ables useful for distinguishing the signal from the background, discussed in Sec. 1.3.5, and evaluate their combined performance on the signal selection. I choose the cut values that result in the best statistical significance, based on a chosen Figure Of Merit (FOM). Given that we are searching for a very limited number of signal events on top of a large background, I chose a simple statistics-only FOM

$$\text{FOM} = \frac{\text{Signal}}{\sqrt{\text{Background}}}. \quad (1.39)$$

The summary of the cut values for the event selection of neutrino magnetic moment signal is presented in Tab. 1.2, showing the label for the event selection variable, its description and the cut value chosen. After the full event selection, the predicted number of signal events for  $\mu_\nu = 10^{-9} \mu_B$  is 56.80 and the total number of background events under the SM hypothesis is 700.33.

### 1.3.1 Data Collection Quality

To ensure good data quality, we apply the following criteria to data (not applied to simulation) [30]. A cut on the time of each spill relative to other spills and on the exposure of each spill, where every spill is required to have at least  $2^{12}$  POT. Additionally, the current in the focusing horn is required to be within  $-202 \text{ kA} < I_{Horn} < -196.4 \text{ kA}$ , the position of the beam to be within  $\pm 2 \text{ cm}$  in both x and y axis, and that the width of the beam to be within 0.57 and 1.58 cm. Furthermore, incomplete events, or events with issues in one or more Data Concentration Modules (DCMs) are removed.

### 1.3.2 Reconstruction Quality

As described in Sec. ??, electrons are reconstructed by slicing, then vertexing, then clustering into prongs. To identify electrons we require a valid reconstructed vertex and at least one reconstructed prong. Even though electrons only consist of a single shower, we don't reject events with more than one prong in a slice, as the reconstruction can wrongly assign noise hits as a separate prong. These false secondary prongs can be removed later in the event selection.

Figure 1.6 and Tab. 1.3 show that about 68 % of signal events do not have a valid

reconstructed vertex. This is due to the concentration of signal events at very low electron recoil energies, which results in events that can consist of a small number of hits, or even a single hit. As can be seen in the bottom plot in Fig. 1.6, events with small true electron recoil energies have much smaller vertex reconstruction efficiency than the higher energetic electrons. However, ongoing work is improving the vertex

Table 1.2: Summary of the variables and their cut values for the event selection of neutrino magnetic moment signal. Showing the category of the event selection variable, its label, description and the cut value chosen.

	Label	Description	Cut
<b>Reco Qual.</b>	<b>Valid Vtx</b>	Valid reconstructed vertex	$> 0$
	<b>N° Prongs</b>	Number of reconstructed prongs	$> 0$
	<b>Hits / Plane</b>	Number of hits per plane	$< 6$
	<b>Low <math>E_{Shower}</math></b>	Low cut on calorimetric energy of the most energetic shower	$> 0.5 \text{ GeV}$
<b>Pre-selection</b>	<b>N° Hits Loose</b>	Preliminary cut on the total number of hits for all prongs in a slice	$< 280$
	<b>Prong Length</b>	Length of the longest prong	$< 640 \text{ cm}$
	<b><math>E\theta^2</math> Loose</b>	Preliminary cut on the product of the calorimetric energy and angle squared of the leading shower	$< 0.064 \text{ GeV} \times \text{rad}^2$
<b>Fiducial</b>	<b>Vertex</b>	x position	$> -177 \text{ cm}$ $< 177 \text{ cm}$
		y position	$> -177 \text{ cm}$ $< 177 \text{ cm}$
		z position	$> 50 \text{ cm}$
			$< 1170 \text{ cm}$
<b>Containment</b>	<b>Prong</b>	Minimum hit position in x	$> -177 \text{ cm}$
		Maximum hit position in x	$< 177 \text{ cm}$
		Minimum hit position in y	$> -185 \text{ cm}$
		Maximum hit position in y	$< 177 \text{ cm}$
		Minimum hit position in z	$> 55 \text{ cm}$
		Maximum hit position in z	$< 1270 \text{ cm}$
<b>Selection</b>	$E_{Shower}/E_{Tot}$	Fraction of energy contained in the most energetic shower	$> 0.91$
	<b>N° Hits</b>	Total number of hits for all prongs in a slice	$< 116$
	<b>High <math>E_{Shower}</math></b>	Calorimetric energy of the most energetic shower	$< 1.4 \text{ GeV}$
	<b><math>\nu</math>-on-e ID</b>	Convolutional Visual Network (CVN)-based $\nu$ -on-e identifier	$> 0.65$
	<b><math>E\pi^0</math> ID</b>	CVN-based $\nu$ -on-e and $\pi^0$ identifier	$> 0.63$
	$E\theta^2$	Product of the calorimetric energy and angle squared of the leading shower	$< 0.0048 \text{ GeV} \times \text{rad}^2$

reconstruction in the **NOvA** detectors with a use of Machine Learning (ML) instead of the currently used Hough transform combined with Elastic Arms [31]. Improving **NOvA** vertex reconstruction at low energies can enhance our event selection in the future.

Additionally, we limit the number of hits per plane to  $< 6$ . This is to remove the so-called ‘Front End Board (FEB) flashers’, which are caused by such a high energy deposit in one cell, that it affects all the other channels on the same Avalanche Photodiode (APD) [32]. The cut value was chosen so that it removes approximately 0.25 % signal events, which is the same criterion as is used for the pre-selection cuts described below. Relative comparisons between signal and background for the number of prongs and the number of hits per plane are shown in Fig. 1.7.

Furthermore, the reconstructed calorimetric energy of the primary shower is required to be  $E_{cal} > 0.5 \text{ GeV}$  as shown in Fig. 1.8. This is primarily due to the limitations of the currently used **CVN**-based  $\nu$ -on-e identifiers described in Sec. 1.3.5, which were developed and validated for  $\nu$ -on-e events with energies above this limit, to avoid the large background at low energies. However, due to the nature of the neutrino magnetic moment signal, which is concentrated at low electron recoil energies, this cut also removes a majority of our signal events, specifically 66.8 %. This large reduction severely impacts the significance of our measurement. On the other hand, it also marks potentially the most impactful improvement available in a future re-analysis. There are other event identifying algorithms available in **NOvA** that could be explored for  $\nu$ -on-e events to leverage the low energy sample. Additionally, it is possible to develop a purpose-built  $\nu$ -on-e identifier focusing on low electron recoil energies.

### 1.3.3 Pre-Selection

Pre-selection aims to remove obvious background events without significantly affecting the signal. The criterion we chose for the selection of these cuts is determined by the reduction of the signal efficiency by approximately 0.25 % with each cut. This results in the total pre-selection reduction of the signal efficiency by approximately 1 %.

The first two variables used for our pre-selection are the same as were used in the

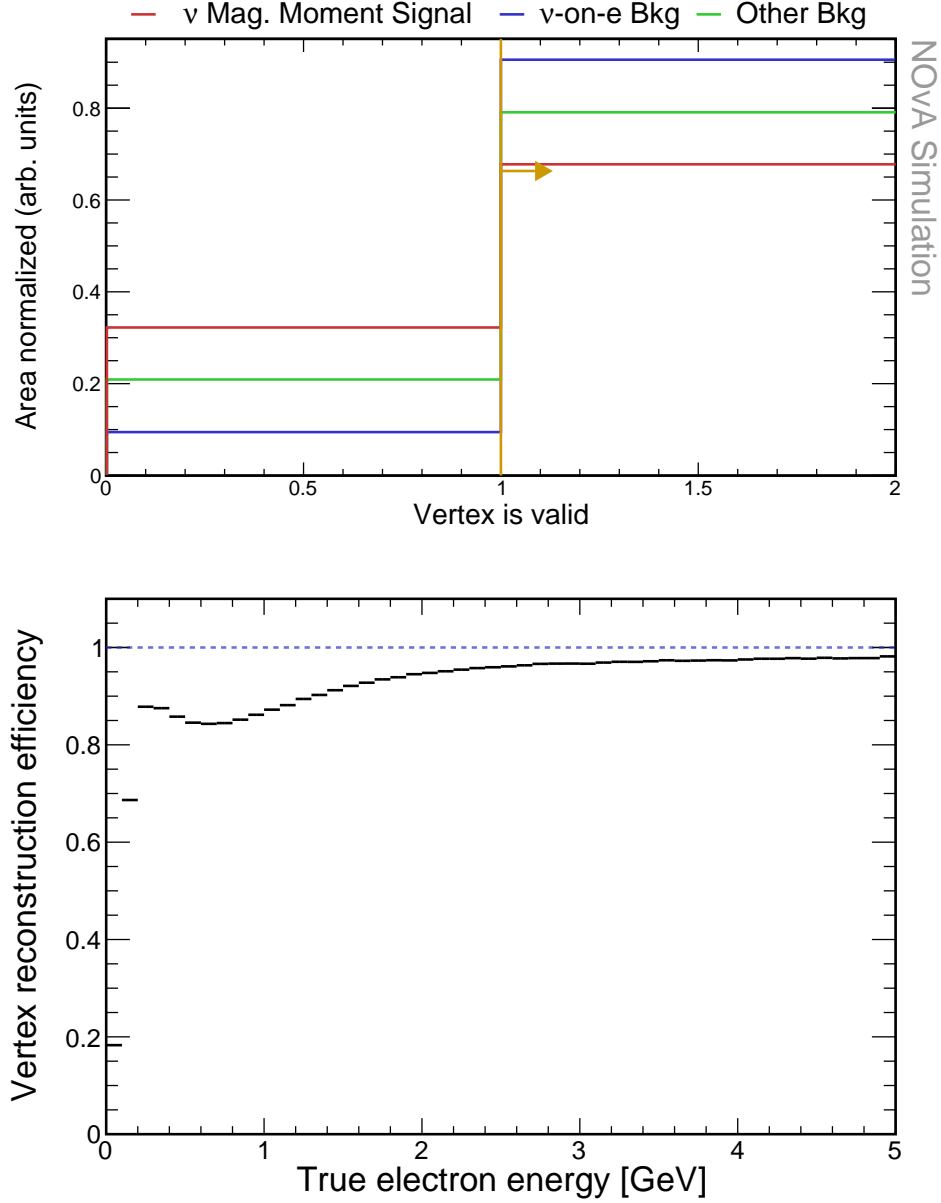


Figure 1.6: Top: Relative comparison of the signal (red),  $\nu$ -on-e background (blue), and other background (green) events for the vertex reconstruction quality selection. Each histogram is area-normalised and the first bin corresponds to events without a valid vertex and second bin to events with correctly reconstructed vertex. The yellow line indicates the chosen cut value, where all events have to have a valid reconstructed vertex. Bottom: profile histogram of the ‘vertex is valid’ variable as a function of the true electron energy for the true signal events, showing the significant drop in vertex reconstruction efficiency at low electron recoil energies. No selection was applied prior to making these plots.



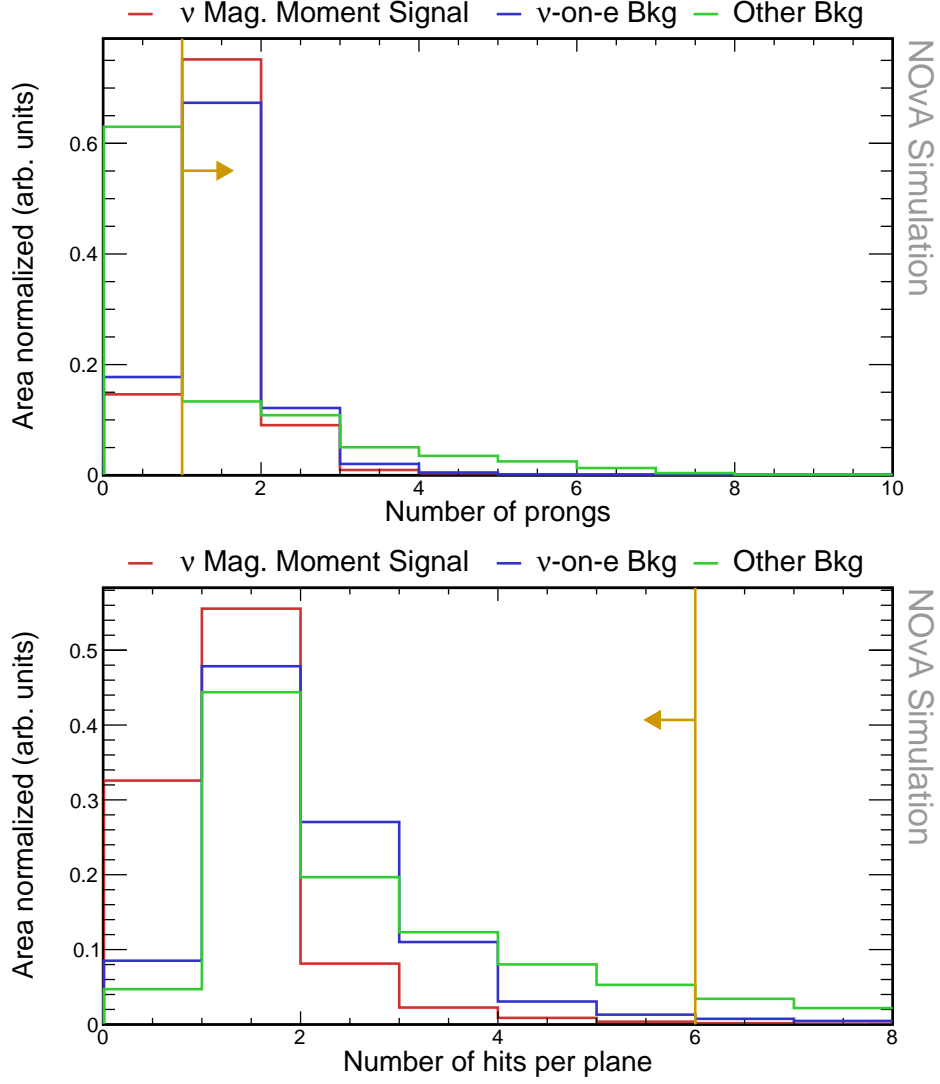


Figure 1.7: Relative comparison of signal (red),  $\nu$ -on-e background (blue), and other background (green) events in the number of prongs (top) and the number of hits per plane (bottom) distributions. Events in both plots are required to have a valid reconstructed vertex and in the bottom plot also at least one reconstructed prong. Yellow lines indicate the cut values for the shown variables, with arrows pointing towards the preserved events. All histograms are area-normalised.

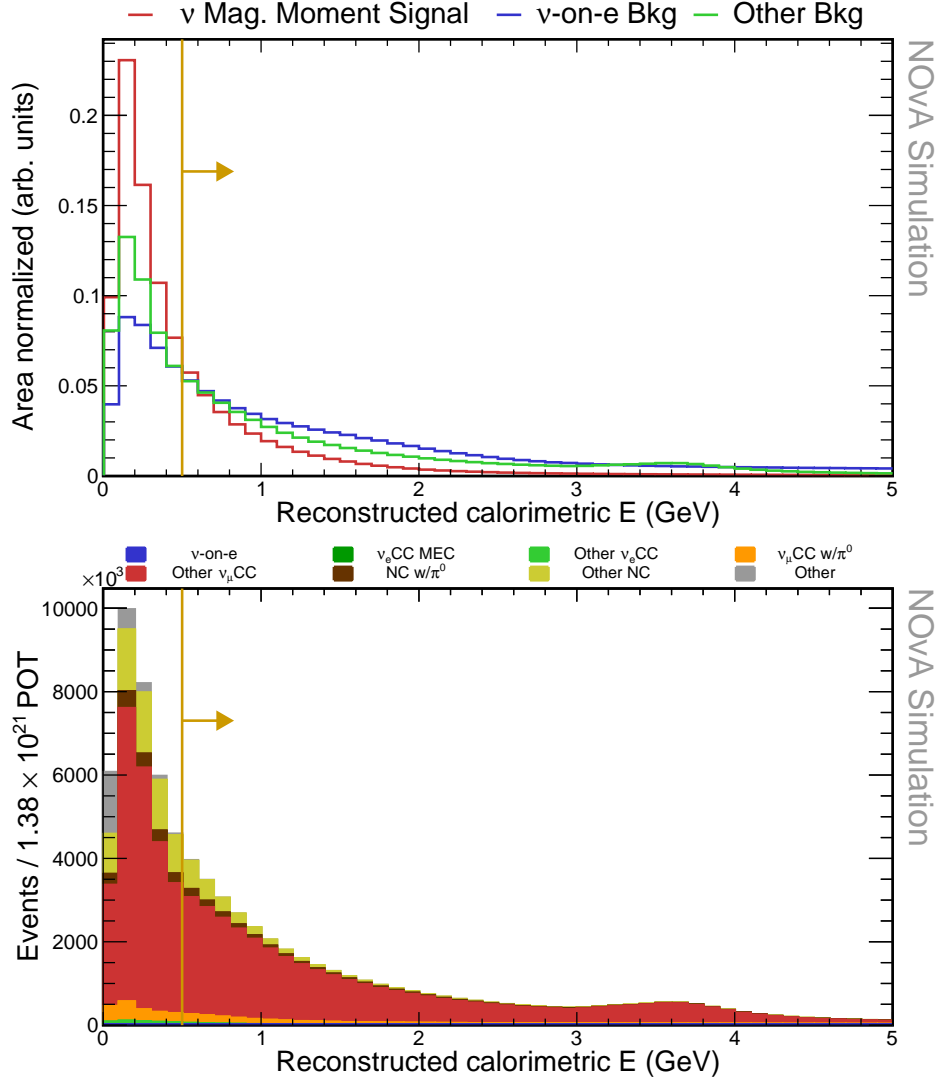


Figure 1.8: Top: Relative comparison of signal (red),  $\nu$ -on-e background (blue), and other background (green) events in the reconstructed calorimetric energy distribution. All histograms are area-normalised. Bottom: Decomposition of background into various sub-samples, normalised to the data POT exposure. Events in both plots are required to have a valid reconstructed vertex, at least one reconstructed prong and less than 6 hits per plane. Yellow lines indicate the cut value for the reconstructed calorimetric energy, with arrows pointing towards the preserved events.

event selection for the  $\nu_e$  appearance ND constraint for the three flavour neutrino oscillation measurements [26]. As we are searching for single electron showers, we can reduce backgrounds with multiple final state particles by limiting the total activity in the detector. Specifically, we require that the total number of hits assigned to all the reconstructed prongs is  $< 280$ . This is shown in Fig. 1.9. In general, the main background in NOvA consists of the  $\nu_\mu$ CC interactions, which are characterised by long muon tracks. We therefore limit the length of the longest reconstructed prong to be  $< 640$  cm, as shown in Fig. 1.10.

Additionally, as discussed in Sec. 1.1.2, simple  $2 \rightarrow 2$  kinematics dictate that the true electron recoil energy and angle for the  $\nu$ -on-e interaction are limited by  $E\theta^2 < 2m_e$ . This can be used to distinguish  $\nu$ -on-e elastic scattering from  $\nu_e$ CC interactions, which also have an electron in the final state. However, due to unavoidable reconstruction deficiencies, the reconstructed  $E\theta^2$  does not have such a strict cut-off value, and we are placing the pre-selection cut at  $E\theta^2 < 0.064$ , as can be seen in Fig. 1.11. Furthermore, some of the signal events can be reconstructed with the opposite direction with respect to the beam, which would result in  $\theta \approx \pi$  rad. However, this reconstruction failure likely does not impact other reconstructed qualities and these events should be preserved for the final sample. For that reason, we are calculating the angle between the outgoing electron and the neutrino beam direction as  $\arccos(\text{abs}(\cos \theta))$ , which gives the same value whether the shower is reconstructed forward or backwards.

The effect of the pre-selection cuts on the signal and background samples are summarised in Tab. 1.4, where the first row lists the number of events after applying

Table 1.3: Event selection cutflow table for the reconstruction quality cuts showing the number of events and the relative efficiency of each cut for each signal sample. The relative efficiency is calculated as number of events remaining after applying the corresponding cut divided by number of events for all the previous cuts. All the cuts are listed in sequence as they are applied.

Selection	Signal		$\nu$ -on-e bkg		Other bkg	
	$N_{evt}$	$\epsilon_{rel} (\%)$	$N_{evt}$	$\epsilon_{rel} (\%)$	$N_{evt}$	$\epsilon_{rel} (\%)$
<b>No Cut</b>	817.34	100	$6.82 \times 10^3$	100	$2.96 \times 10^8$	100
<b>Valid Vtx</b>	553.86	67.76	$6.17 \times 10^3$	90.55	$2.34 \times 10^8$	79.10
<b>N<sup>o</sup> Prongs</b>	472.90	85.38	$5.08 \times 10^3$	82.25	$8.66 \times 10^7$	37.00
<b>Hits / Plane</b>	471.14	99.63	$4.97 \times 10^3$	97.85	$7.32 \times 10^7$	89.56
<b>Low <math>E_{Shower}</math></b>	156.37	33.19	$3.53 \times 10^3$	71.09	$4.06 \times 10^7$	55.12

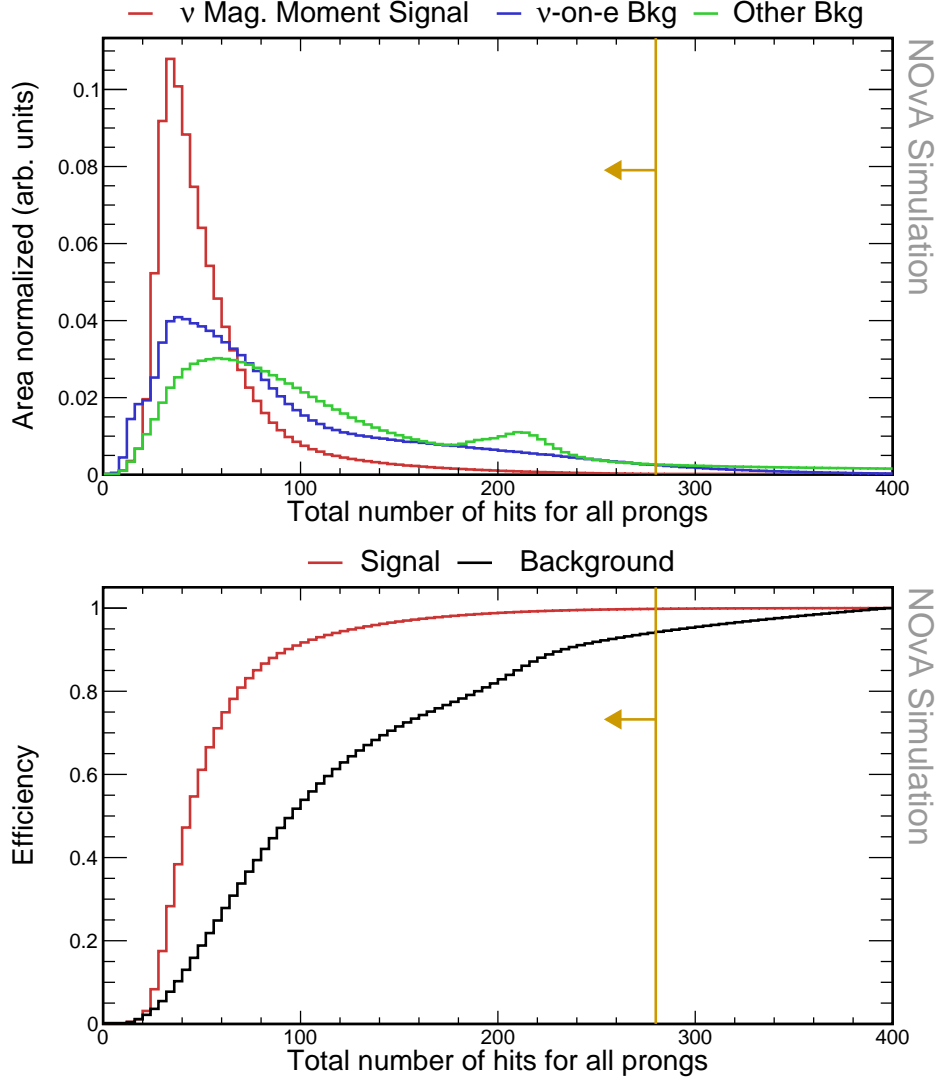


Figure 1.9: Top: Relative comparison of signal (red),  $\nu$ -on-e background (blue), and other background (green) events in the distribution of total number of hits from all reconstructed prongs in the slice. All histograms are area-normalised. Bottom: Cumulative signal (red) and background (black) efficiency calculated as number of signal/background events left of the bin divided by the total number of signal/background events. Yellow lines indicate the cut value for the maximum number of hits, with arrows pointing towards the preserved events. The reconstruction quality cuts were applied before making these plots.

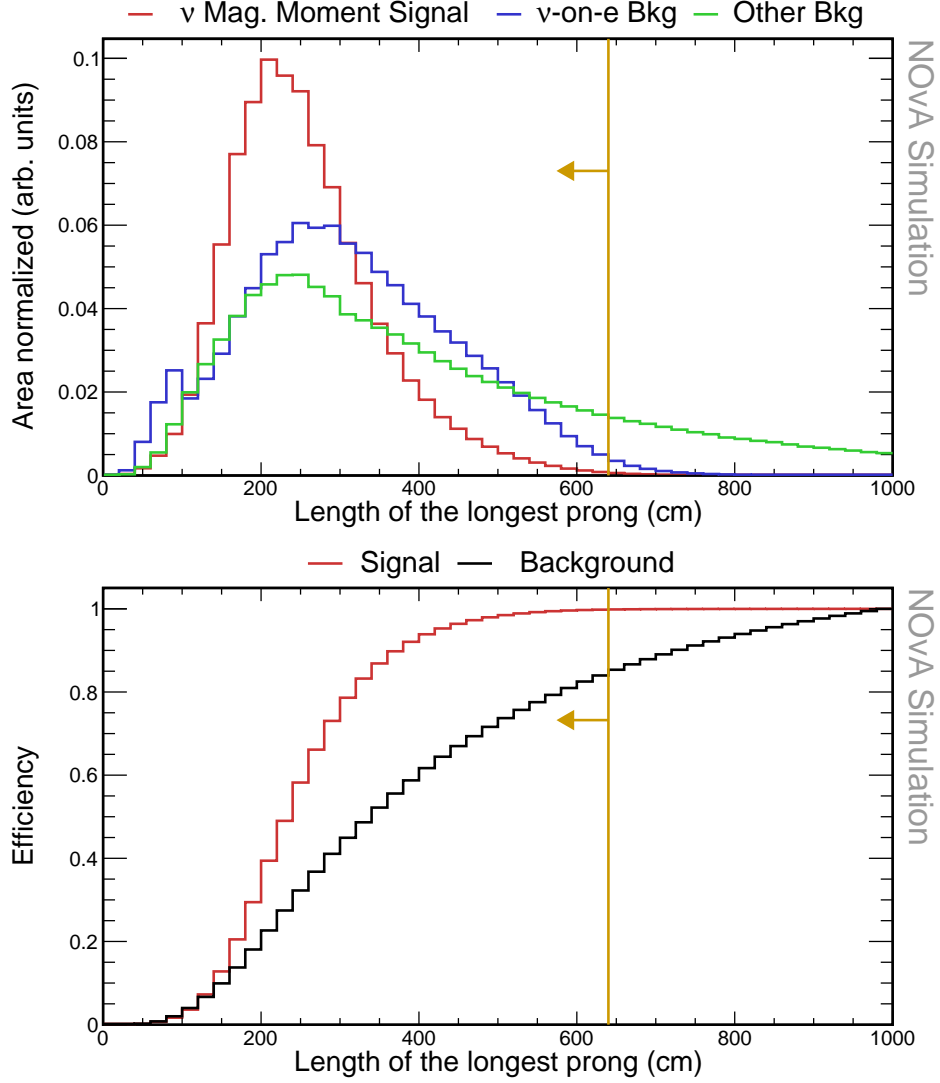


Figure 1.10: Top: Relative comparison of signal (red),  $\nu$ -on- $e$  background (blue), and other background (green) events in the distribution of the length of the longest reconstructed prong in slice. All histograms are area-normalised. Bottom: Cumulative signal (red) and background (black) efficiency calculated as number of signal/background events left of the bin divided by the total number of signal/background events. Yellow lines indicate the cut value for the maximum length of the longest prong, with arrows pointing towards the preserved events. The reconstruction quality cuts and the number of hits cut were applied before making these plots.

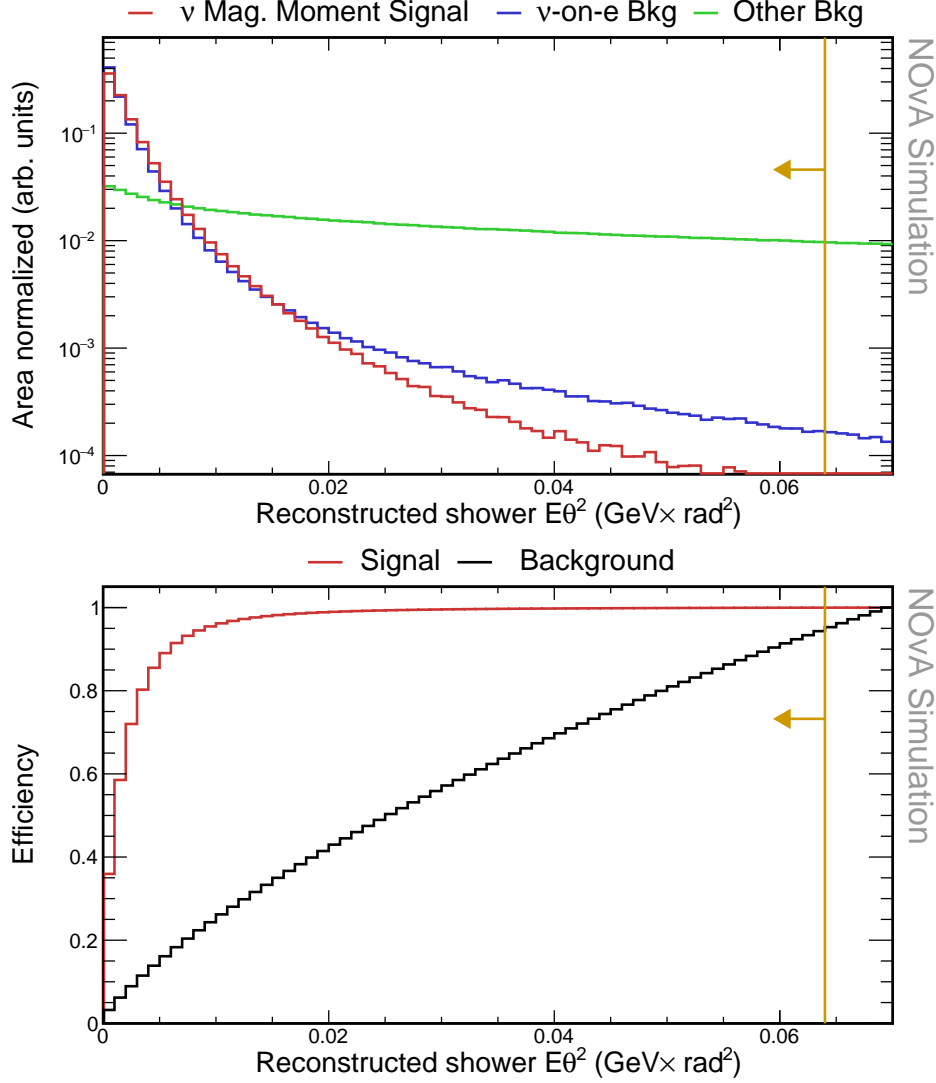


Figure 1.11: Top: Relative comparison of signal (red),  $\nu$ -on- $e$  background (blue), and other background (green) events in the distribution of the reconstructed energy of the leading shower multiplied by its angle from the incoming neutrino beam direction squared. All histograms are area-normalised with logarithmic y axis. Bottom: Cumulative signal (red) and background (black) efficiency calculated as number of signal/background events left of the bin divided by the total number of signal/background events. Yellow lines indicate the cut value for the depicted variable, with arrows pointing towards the preserved events. The reconstruction quality cuts, the number of hits cut, and the length of the longest prong cuts were applied before making both of these plots.

all the reconstruction quality cuts from Sec. 1.3.2. All three of the variables used for the pre-selection are employed again in the MVA, as described in Sec. 1.3.5.

Table 1.4: Pre-selection cutflow table showing the number of events and the relative efficiency of each cut for each signal sample. The relative efficiency is calculated as number of events remaining after applying the corresponding cut divided by number of events for all the previous cuts. All the cuts are listed in sequence as they are applied. The top row corresponds to the sample after applying the reconstruction quality cuts.

Selection	Signal		$\nu$ -on-e bkg		Other bkg	
	$N_{evt}$	$\epsilon_{rel} (\%)$	$N_{evt}$	$\epsilon_{rel} (\%)$	$N_{evt}$	$\epsilon_{rel} (\%)$
<b>Reco Quality</b>	156.37	100	$3.53 \times 10^3$	100	$4.28 \times 10^7$	100
<b>N° Hits Loose</b>	156.05	99.79	$3.41 \times 10^3$	96.46	$3.61 \times 10^7$	84.35
<b>Prong Length</b>	155.7	99.78	$3.37 \times 10^3$	98.85	$2.61 \times 10^7$	72.36
<b><math>E\theta^2</math> Loose</b>	155.14	99.64	$3.33 \times 10^3$	98.83	$8.83 \times 10^6$	33.82

### 1.3.4 Fiducial and Containment Cuts

To ensure all the deposited energy of the recoil electron is contained within the detector and to remove events originating outside of the detector (such as rock muons for the ND), we constrain the position of the reconstructed vertex and all the prongs in the slice. The decision on where to place the exact cut values is made based on the maximum FOM value.

The reconstructed vertex is required to be within the fiducial volume, which represents a well-understood volume of the detector. To select the fiducial volume, we investigate distributions of the reconstructed vertex in the x, y and z direction, shown in Fig. 1.12, 1.13 and 1.14 respectively. Basic reconstruction quality and pre-selection cuts are applied to make these distributions. Additionally, for the x and y position distributions, we require that the vertex is not placed inside of the Muon Catcher by requiring  $Vtx_z < 1270$  cm, as it can significantly affect these distributions. The slanted distributions in x and y are caused by the off-axis nature of the Neutrinos from the Main Injector (NuMI) beam and the periodic peaks are due to a combination of the detector structure and the choice of binning.

The reconstructed vertex is required to be contained within the following volume:

$$-175 \text{ cm} < Vtx_X < 175 \text{ cm}, \quad (1.40)$$

$$-175 \text{ cm} < Vtx_Y < 175 \text{ cm}, \quad (1.41)$$

$$95 \text{ cm} < Vtx_Z < 1170 \text{ cm}. \quad (1.42)$$

Furthermore, we constrain the extreme positions (minimum and maximum) of all the hits within the most energetic prong, which is assumed to represent the electron shower for the signal events. We apply the reconstruction quality, pre-selection and fiducial (vertex position) cuts to their distributions, shown in Fig. 1.15-1.20. The extreme hit positions are required to be within the following volume:

$$-175 \text{ cm} < \min_X, \max_X < 175 \text{ cm}, \quad (1.43)$$

$$-175 \text{ cm} < \min_Y, \max_Y < 175 \text{ cm}, \quad (1.44)$$

$$105 \text{ cm} < \min_Z, \max_Z < 1270 \text{ cm}. \quad (1.45)$$

Table 1.5: Event selection cutflow table for the containment cuts showing the number of events and the relative efficiency of each cut for each signal sample. The relative efficiency is calculated as number of events remaining after applying the corresponding cut divided by number of event for all the previous cuts. All the cuts are listed in sequence as they are applied. The top row corresponds to the sample after applying the reconstruction quality and pre-selection cuts.

Selection	Signal		$\nu$ -on-e bkg		Other bkg	
	$N_{evt}$	$\epsilon_{rel} (\%)$	$N_{evt}$	$\epsilon_{rel} (\%)$	$N_{evt}$	$\epsilon_{rel} (\%)$
<b>Pre-selection</b>	155.14	100	$3.33 \times 10^3$	100	$8.83 \times 10^6$	100
<b>Fiducial</b>	143.02	92.19	$2.88 \times 10^3$	85.60	$5.96 \times 10^6$	67.57
<b>Containment</b>	117.41	82.09	$2.08 \times 10^3$	72.12	$1.10 \times 10^6$	18.38

### 1.3.5 Multivariate Analysis Cuts

Following the removal of obvious backgrounds and events not contained within the detector, we aim to optimise the event selection to achieve the highest significance for measuring the effective muon neutrino magnetic moment. This goal is equivalent to maximising our FOM from Eq. 1.39.

For this purpose, we utilised ROOT's [33] Tool for MVA (TMVA) [34]. Specifi-



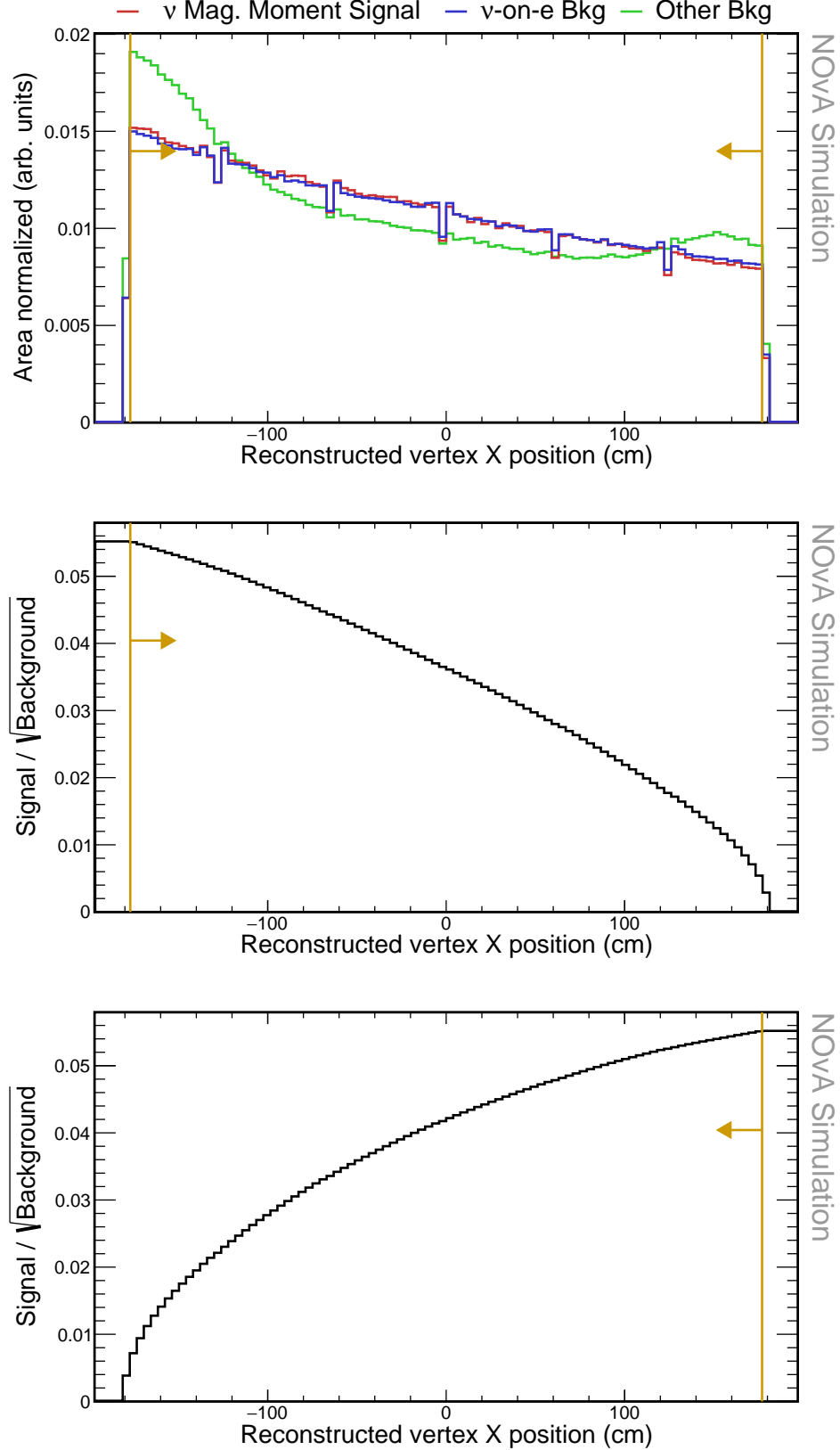


Figure 1.12: Top: Relative comparison of signal (red),  $\nu$ -on-e background (blue), and other background (green) events in the distribution of the x position of the reconstructed vertex. All histograms are area-normalized. Middle and bottom: Cumulative FOM calculated as the number of signal events, divided by the number of background events from that bin until the end of the plot to the right (middle) or left (bottom). The reconstruction quality and pre-selection cuts were applied prior to making these plots. Additionally, vertex is required to be within the active region of the detector ( $Vtx_z < 1270$  cm). Yellow lines show the cut values that create the fiducial volume, with arrows pointing towards the preserved events.

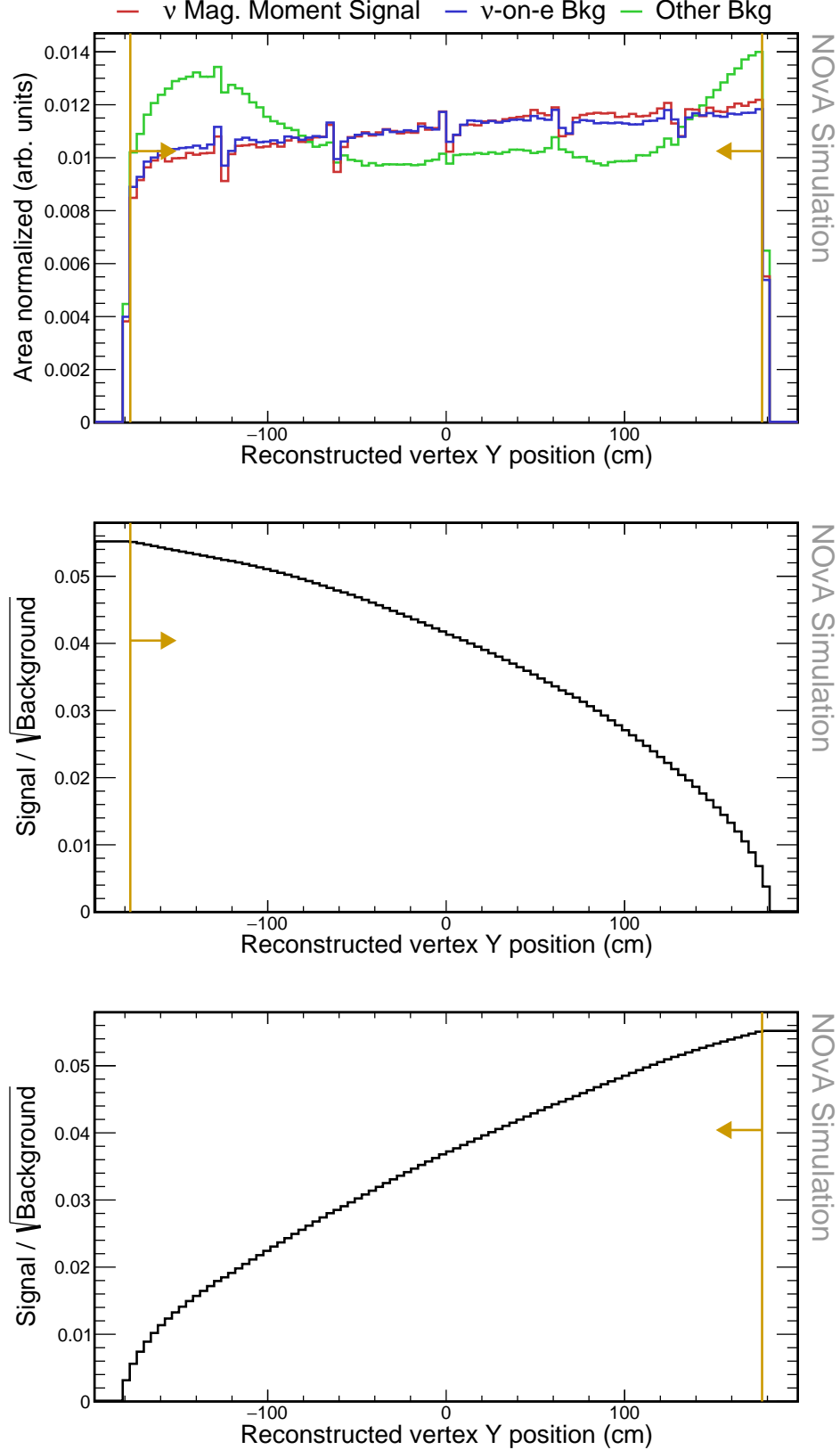


Figure 1.13: Top: Relative comparison of signal (red),  $\nu$ -on-e background (blue), and other background (green) events in the distribution of the y position of the reconstructed vertex. All histograms are area-normalized. Middle and bottom: Cumulative FOM calculated as the number of signal events, divided by the number of background events from that bin until the end of the plot to the right (middle) or left (bottom). The reconstruction quality and pre-selection cuts were applied prior to making these plots. Additionally, vertex is required to be within the active region of the detector ( $Vtx_z < 1270$  cm). Yellow lines show the cut values that create the fiducial volume, with arrows pointing towards the preserved events.

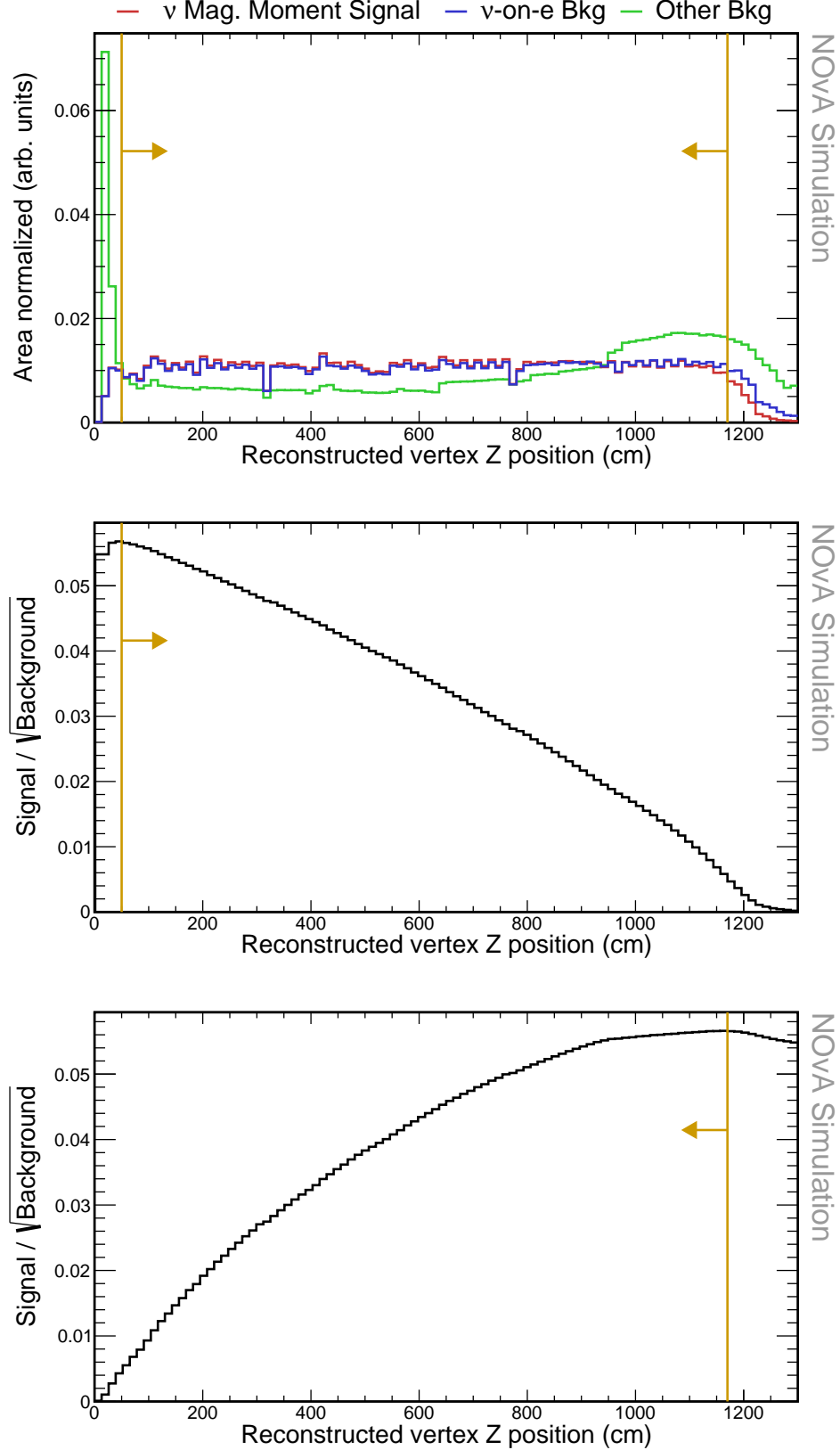


Figure 1.14: Top: Relative comparison of signal (red),  $\nu$ -on-e background (blue), and other background (green) events in the distribution of the z position of the reconstructed vertex. All histograms are area-normalized. Middle and bottom: Cumulative FOM calculated as the number of signal events, divided by the number of background events from that bin until the end of the plot to the right (middle) or left (bottom). The reconstruction quality and pre-selection cuts were applied prior to making these plots. Yellow lines show the cut values that create the fiducial volume, with arrows pointing towards the preserved events.

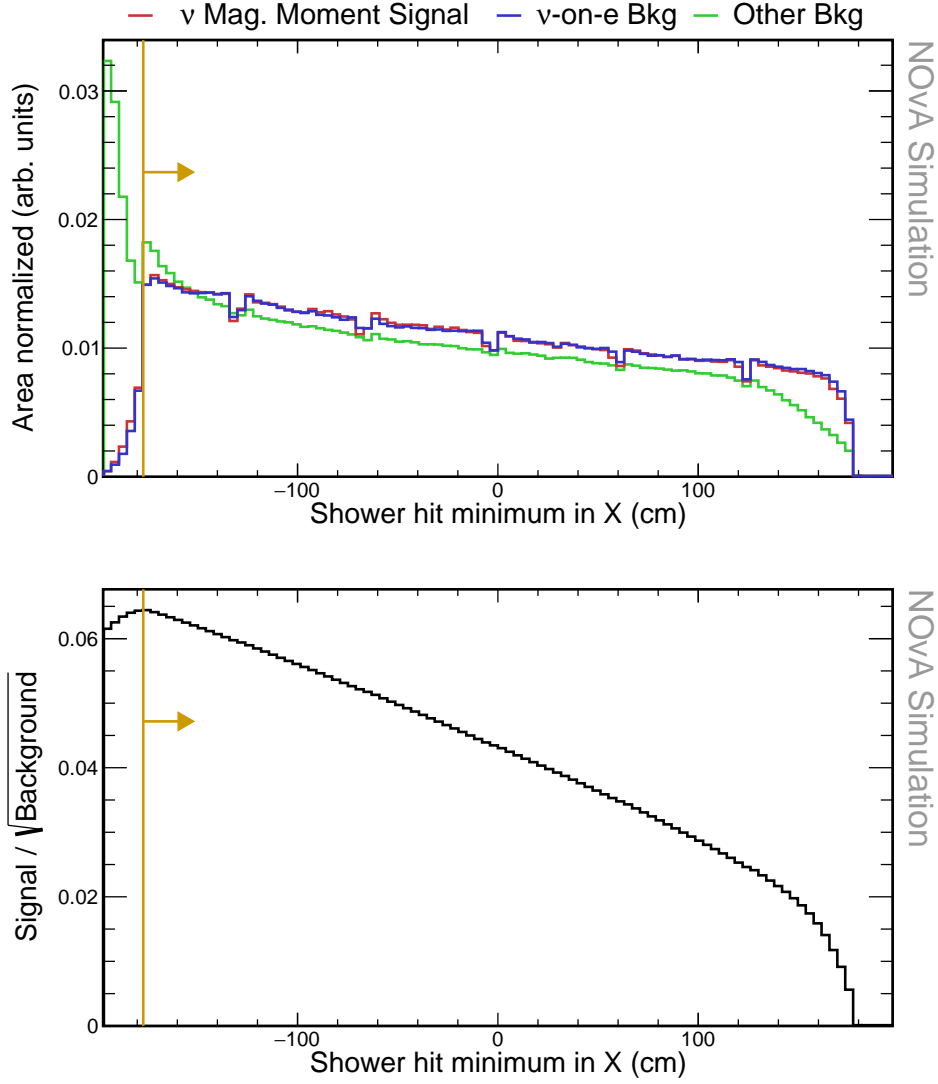


Figure 1.15: Top: Relative comparison of signal (red),  $\nu$ -on- $e$  background (blue), and other background (green) events in the distribution of the minimum hit position of the most energetic prong along the x axis. All histograms are area-normalized. Bottom: Cumulative FOM calculated as the number of signal events, divided by the number of background events from that bin until the end of the plot in the direction of the yellow arrow. The reconstruction quality, pre-selection and fiducial cuts were applied prior to making these plots. Yellow lines show the cut values that create the containment volume, with arrows pointing towards the preserved events.

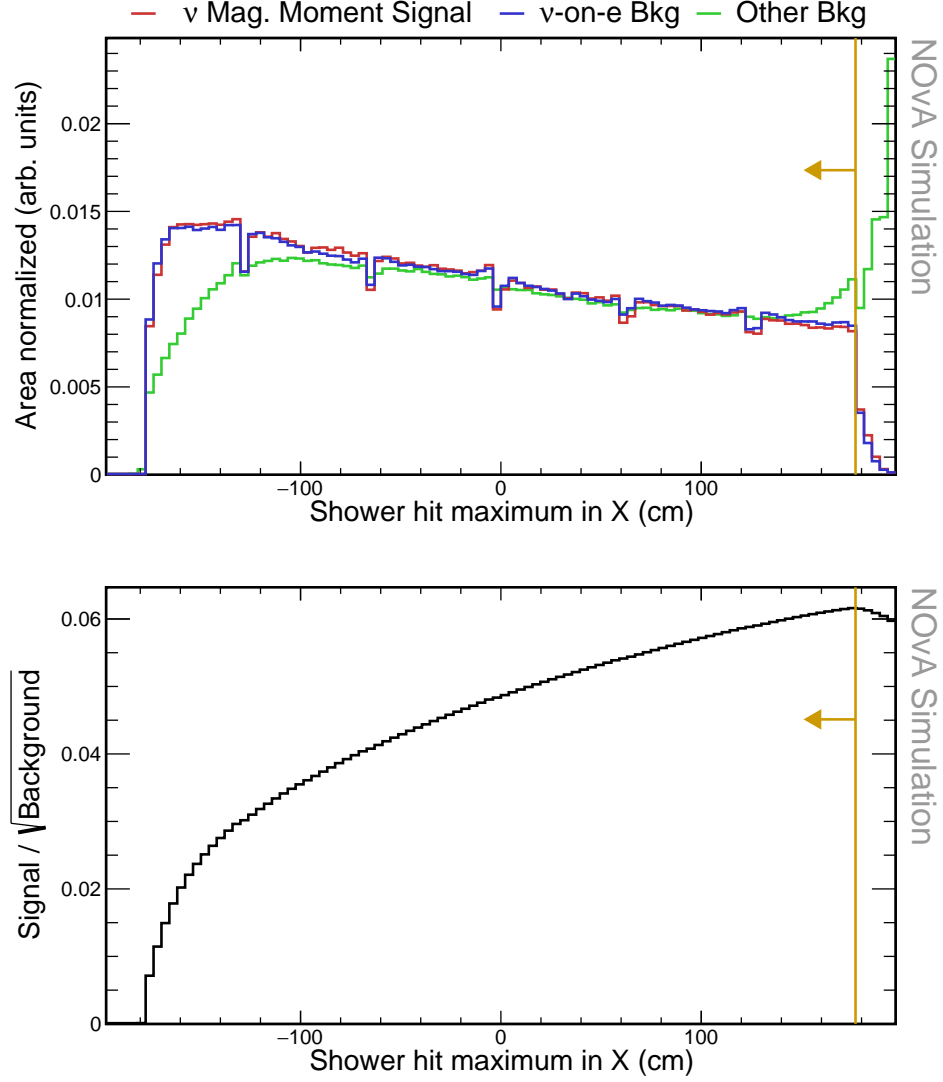


Figure 1.16: Top: Relative comparison of signal (red),  $\nu$ -on- $e$  background (blue), and other background (green) events in the distribution of the maximum hit position of the most energetic prong along the x axis. All histograms are area-normalized. Bottom: Cumulative FOM calculated as the number of signal events, divided by the number of background events from that bin until the end of the plot in the direction of the yellow arrow. The reconstruction quality, pre-selection and fiducial cuts were applied prior to making these plots. Yellow lines show the cut values that create the containment volume, with arrows pointing towards the preserved events.

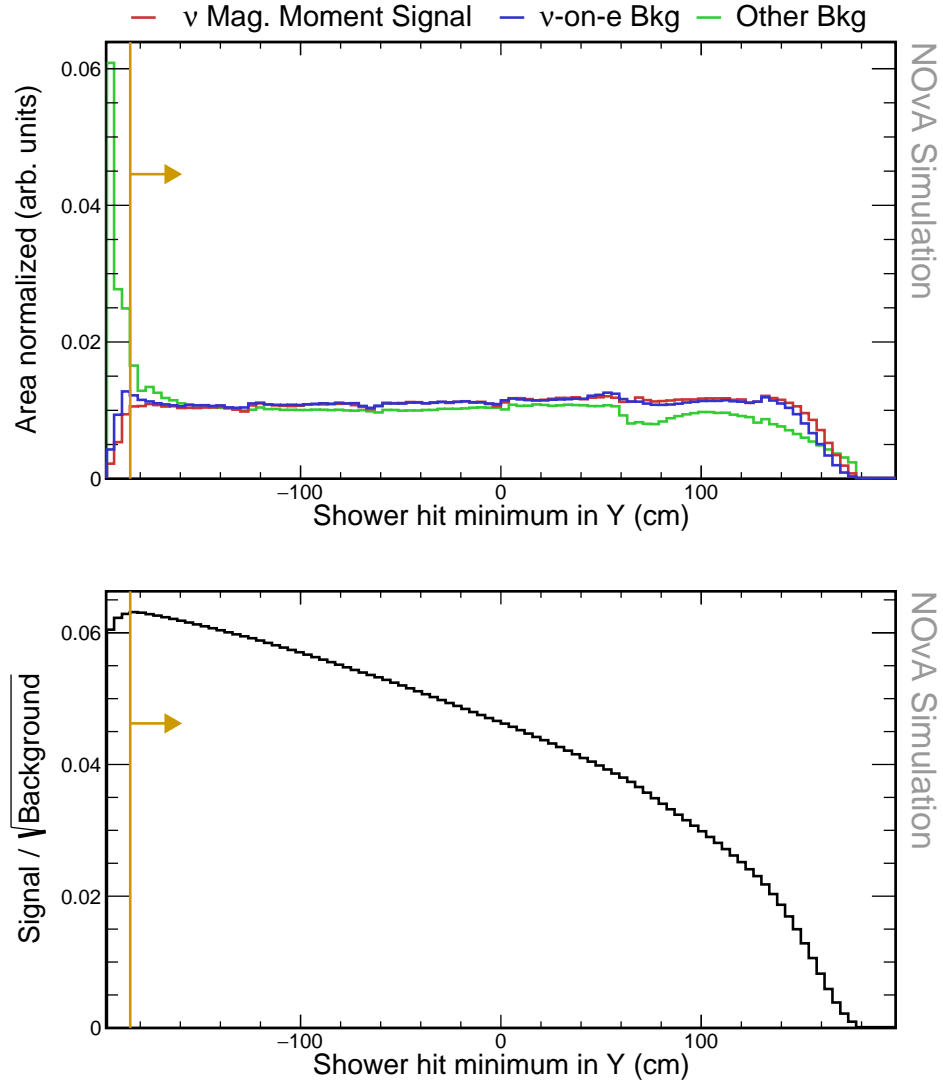


Figure 1.17: Top: Relative comparison of signal (red),  $\nu$ -on- $e$  background (blue), and other background (green) events in the distribution of the minimum hit position of the most energetic prong along the y axis. All histograms are area-normalized. Bottom: Cumulative FOM calculated as the number of signal events, divided by the number of background events from that bin until the end of the plot in the direction of the yellow arrow. The reconstruction quality, pre-selection and fiducial cuts were applied prior to making these plots. Yellow lines show the cut values that create the containment volume, with arrows pointing towards the preserved events.

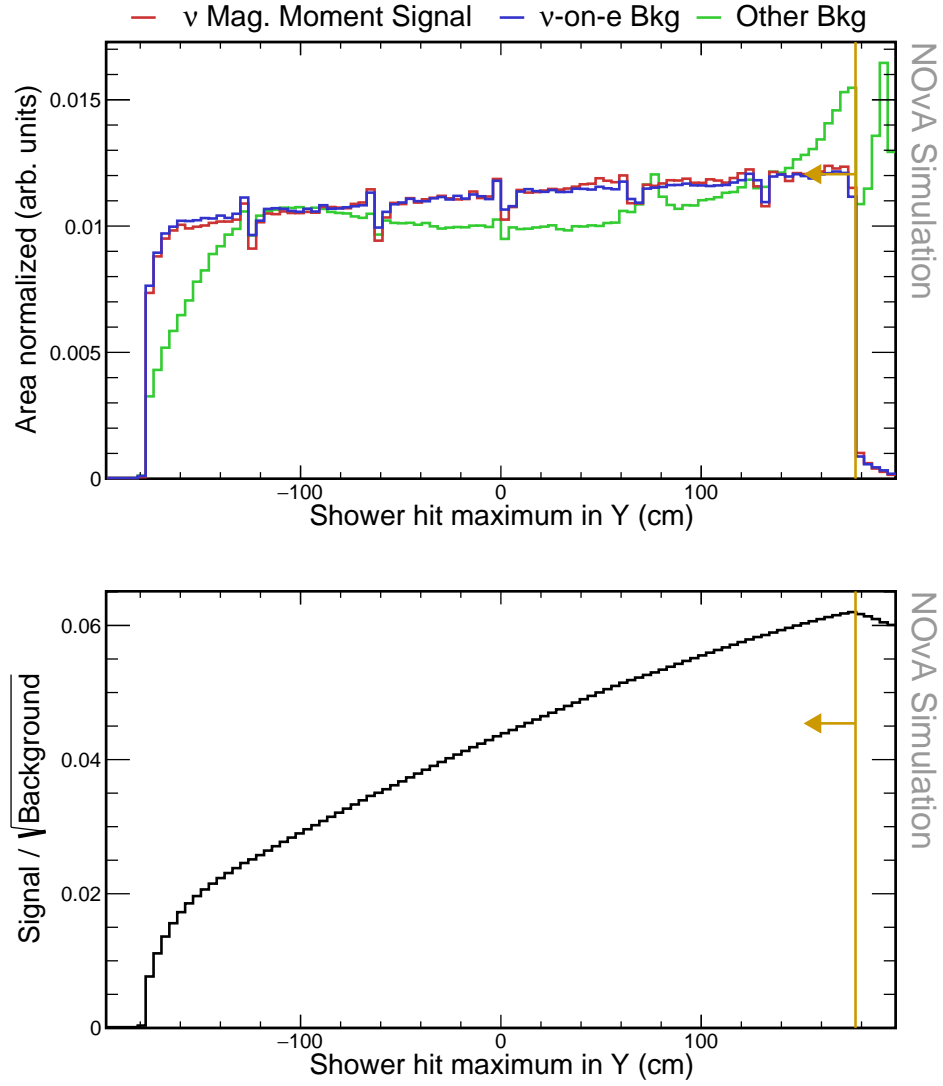


Figure 1.18: Top: Relative comparison of signal (red),  $\nu$ -on- $e$  background (blue), and other background (green) events in the distribution of the maximum hit position of the most energetic prong along the y axis. All histograms are area-normalized. Bottom: Cumulative FOM calculated as the number of signal events, divided by the number of background events from that bin until the end of the plot in the direction of the yellow arrow. The reconstruction quality, pre-selection and fiducial cuts were applied prior to making these plots. Yellow lines show the cut values that create the containment volume, with arrows pointing towards the preserved events.

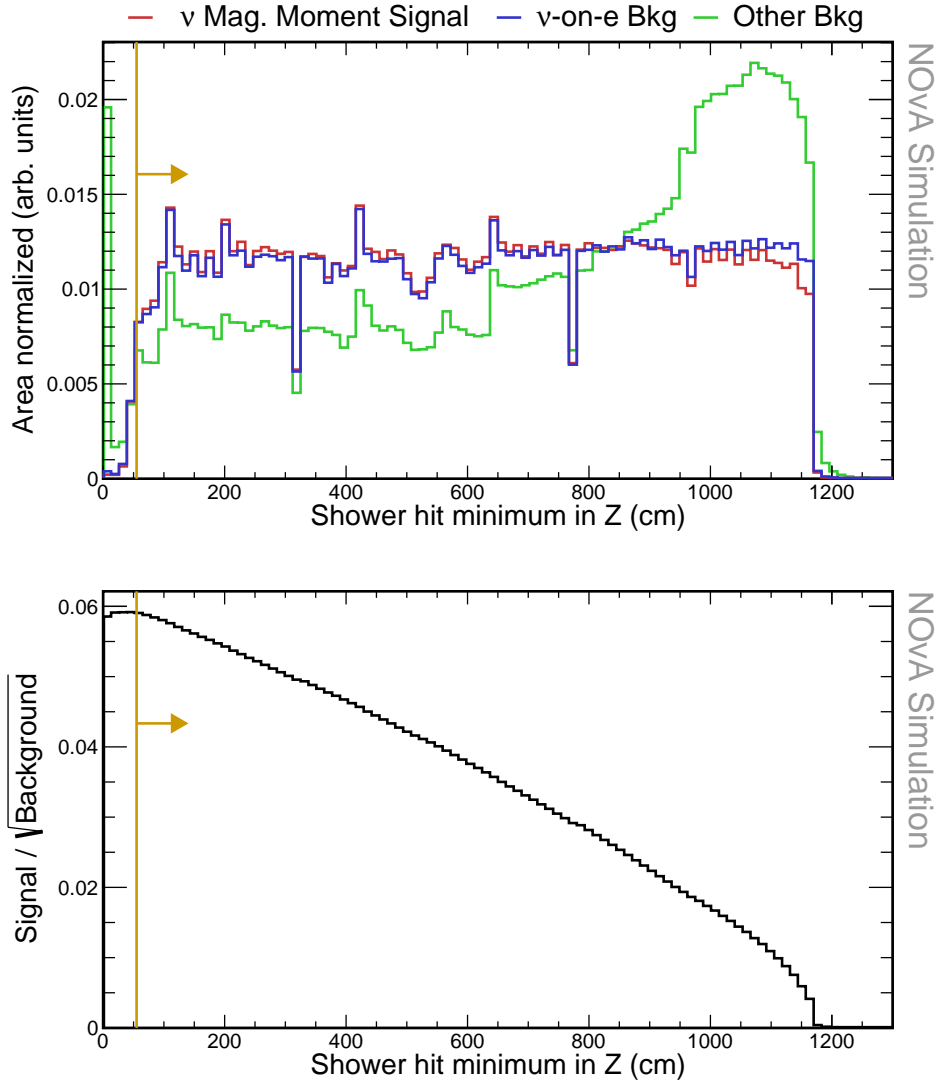


Figure 1.19: Top: Relative comparison of signal (red),  $\nu$ -on- $e$  background (blue), and other background (green) events in the distribution of the minimum hit position of the most energetic prong along the  $z$  axis. All histograms are area-normalized. Bottom: Cumulative FOM calculated as the number of signal events, divided by the number of background events from that bin until the end of the plot in the direction of the yellow arrow. The reconstruction quality, pre-selection and fiducial cuts were applied prior to making these plots. Yellow lines show the cut values that create the containment volume, with arrows pointing towards the preserved events.



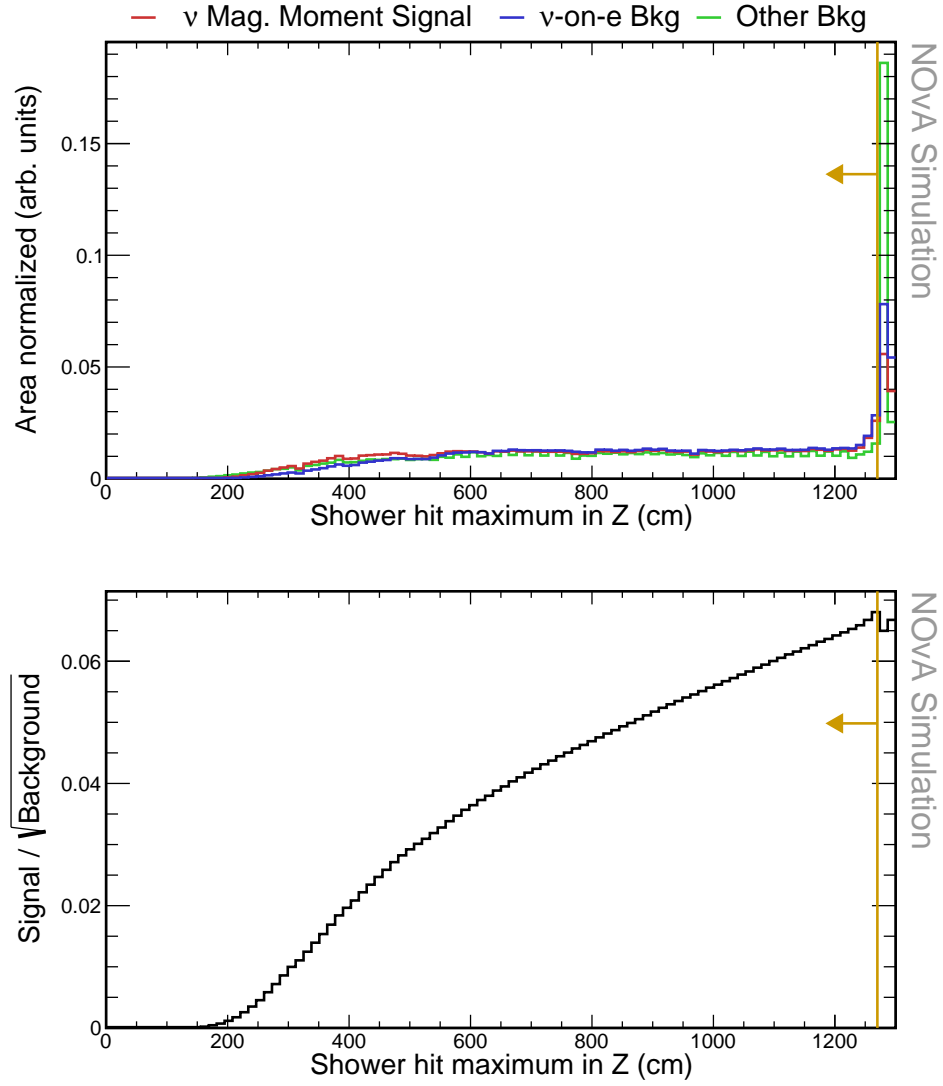


Figure 1.20: Top: Relative comparison of signal (red),  $\nu$ -on- $e$  background (blue), and other background (green) events in the distribution of the maximum hit position of the most energetic prong along the  $z$  axis. All histograms are area-normalized. Bottom: Cumulative FOM calculated as the number of signal events, divided by the number of background events from that bin until the end of the plot in the direction of the yellow arrow. The reconstruction quality, pre-selection and fiducial cuts were applied prior to making these plots. Yellow lines show the cut values that create the containment volume, with arrows pointing towards the preserved events.

cally, we employed the rectangular cut optimisation method, which uses multivariate parameter fitters to maximise background rejection across the full range of signal efficiencies. We used the MC sampling fitting method, assuming that for each input variable, there is a single cut value (maximum or minimum) that optimally discriminates between signal and background.

TMVA generally performs better with a limited number of input variables that have strong discriminating power. Therefore, we investigated several input variables and selected only those that achieved significant background rejection. There are additional variables not mentioned here that might achieve better final results, providing opportunities for future re-analyses. Additionally, we do not apply any transformations to the input variables prior to optimisation, which might also improve the final result after dedicated study.

The variables considered include those already used in the pre-selection: the total number of hits for all prongs in slice, the length of the longest prong, and  $E\theta^2$ , as discussed in Sec. 1.3.3. During the TMVA optimisation, we found that the length of the longest prong did not significantly enhance discriminating power and thus removed it from the set of input variables. Additionally, we included the reconstructed energy of the most energetic shower, as used for reconstruction quality selection in Sec. 1.3.2, intending to restrict events with higher energies, since our signal is concentrated at low electron recoil energies.

Additionally, we considered all the variables used for the NOvA  $\nu$ -on-e analysis for the neutrino flux constraint [13]. The first is the fraction of the reconstructed energy of the most energetic shower ( $E_{Shower}$ ) to the total energy of all the reconstructed prongs in the entire slice ( $E_{Tot}$ ). This variable distinguished our signal events, which only have a single shower, from events with multiple showers or additional activity. The second is the gap between the vertex and the most energetic shower, which can distinguish between electron and  $\pi^0$  events, as the latter should have a characteristic gap several cells long. Additionally, we examined the amount of energy contained within  $\pm 8$  planes away from the vertex, besides the energy associated with the most energetic prong, which should distinguish the purely leptonic signal from backgrounds with significant hadronic activity. However, the gap and the vertex energy variables underperformed compared to others and were ultimately not

used within the TMVA.

We also utilised two Convolutional Neural Network (CNN)-based event classifiers developed for the NOvA  $\nu$ -on-e analysis for the neutrino flux constraint [13, 14]. These classifiers are specifically designed to identify  $\nu$ -on-e interactions. The first, named  $\nu$ -on-eID, is trained to select  $\nu$ -on-e events from the primary  $\nu_\mu$ CC background, while the second, named  $E\pi^0$ ID, is trained on events passing the  $\nu$ -on-eID selection to reject the remaining background with a  $\pi^0$ . These classifiers use a pixel map of the entire slice as input and are designed with the same CNN architecture as ProngCVN and EventCVN described in Sec. ??.

The result of the TMVA is a set of cuts on each of the input variables that maximises the FOM. The input variables and the cuts that were selected for them are shown in Fig. 1.21, 1.22, and 1.23. The effect of these cuts is summarised in Tab. 1.6. Applying the TMVA cuts reduces the signal by 51.62 %, the  $\nu$ -on-e background by 75.03 % and other background by 99.98 %. The specific values of the cuts resulting from the TMVA are

$$E_{Shower}/E_{Tot} > 0.91, \quad (1.46)$$

$$\text{Total } N^o \text{ hits for all prongs} < 116, \quad (1.47)$$

$$E_{Shower} < 1.4 \text{ GeV}, \quad (1.48)$$

$$E\theta^2 < 0.0048 \text{ GeV} \times \text{rad}^2, \quad (1.49)$$

$$\nu - on - eID > 0.65, \quad (1.50)$$

$$E\pi^0ID > 0.63. \quad (1.51)$$

After the full event selection, the predicted number of signal events for  $\mu_\nu = 10^{-9} \mu_B$  is 56.80, and the total number of background events under the SM hypothesis is 700.33. The decomposition of background into interaction types is shown in Fig. 1.24 and listed in Tab. 1.7. The event selection results in

$$\text{Signal Purity} = \frac{\text{Signal}}{\text{Signal} + \text{Background}} = 7.50 \%, \quad (1.52)$$

$$\text{Signal Efficiency} = \frac{\text{Signal}}{\text{Signal}_{\text{No Cut}}} = 6.95 \%. \quad (1.53)$$

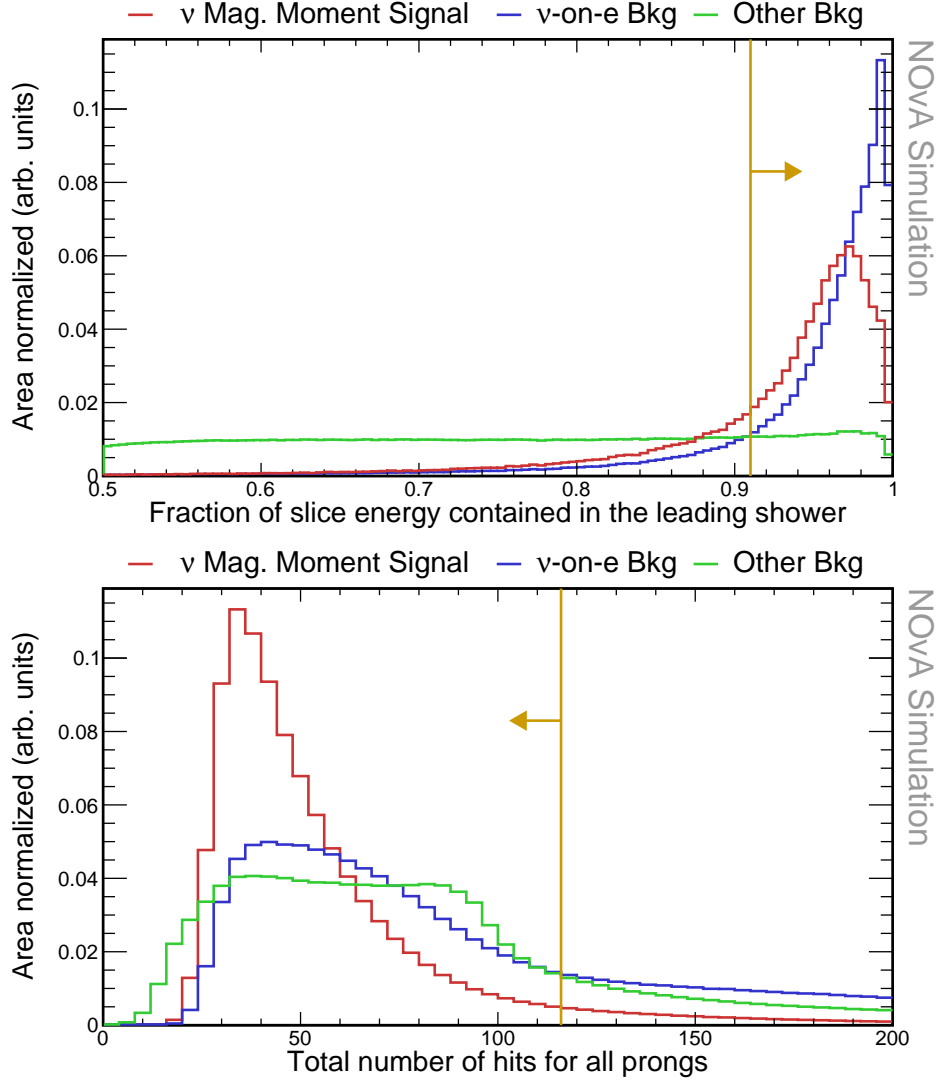


Figure 1.21: Relative comparison of signal (red),  $\nu$ -on-e background (blue), and other background (green) events in the distribution of the fraction of the total energy contained in the primary shower (top) and of the total number of hits in the slice (bottom). All histograms are area-normalized. The reconstruction quality, pre-selection, fiducial and containment cuts were applied prior to making these plots. Yellow lines show the cut values on the depicted variables, with arrows pointing towards the preserved events.

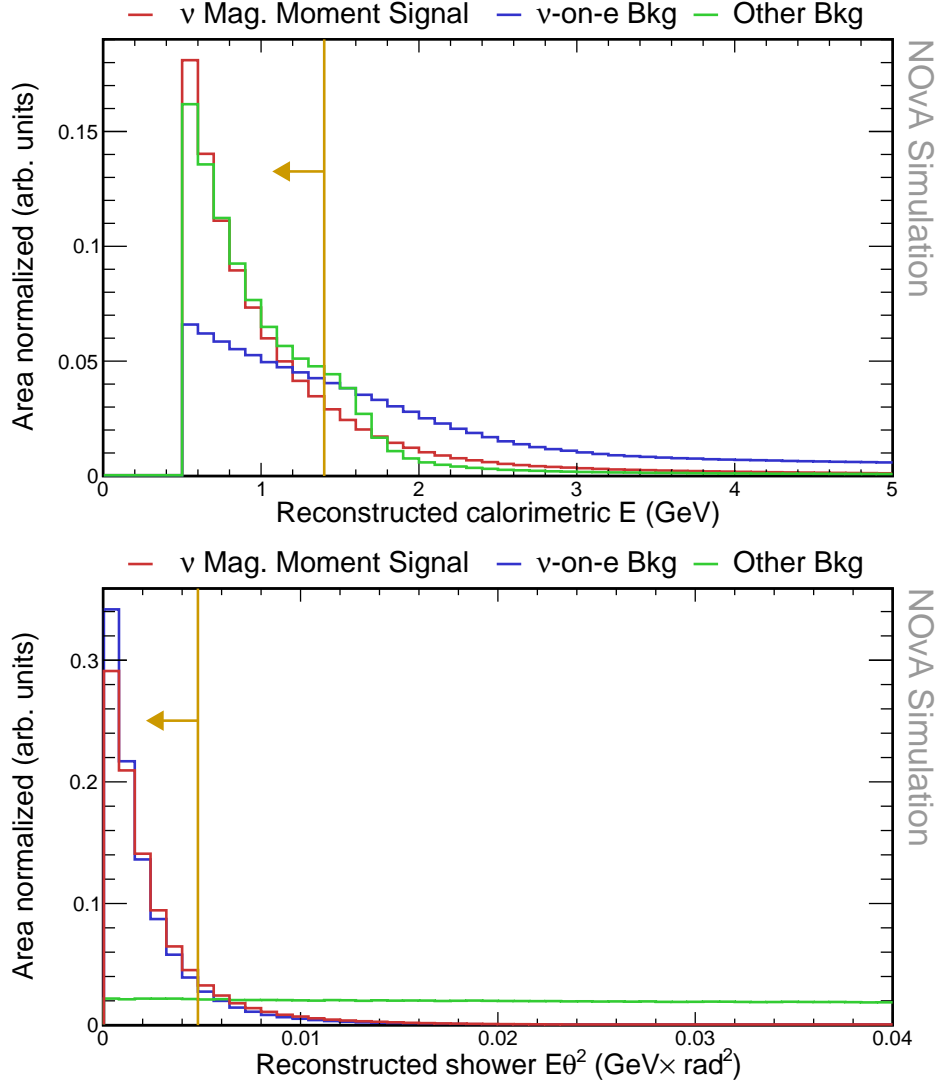


Figure 1.22: Relative comparison of signal (red),  $\nu$ -on-e background (blue), and other background (green) events in the distribution of the reconstructed energy of the primary shower (top) and of the reconstructed energy multiplied by the angle from the incoming neutrino beam direction squared.(bottom). All histograms are area-normalized. The reconstruction quality, pre-selection, fiducial and containment cuts were applied prior to making these plots. Yellow lines show the cut values on the depicted variables, with arrows pointing towards the preserved events.

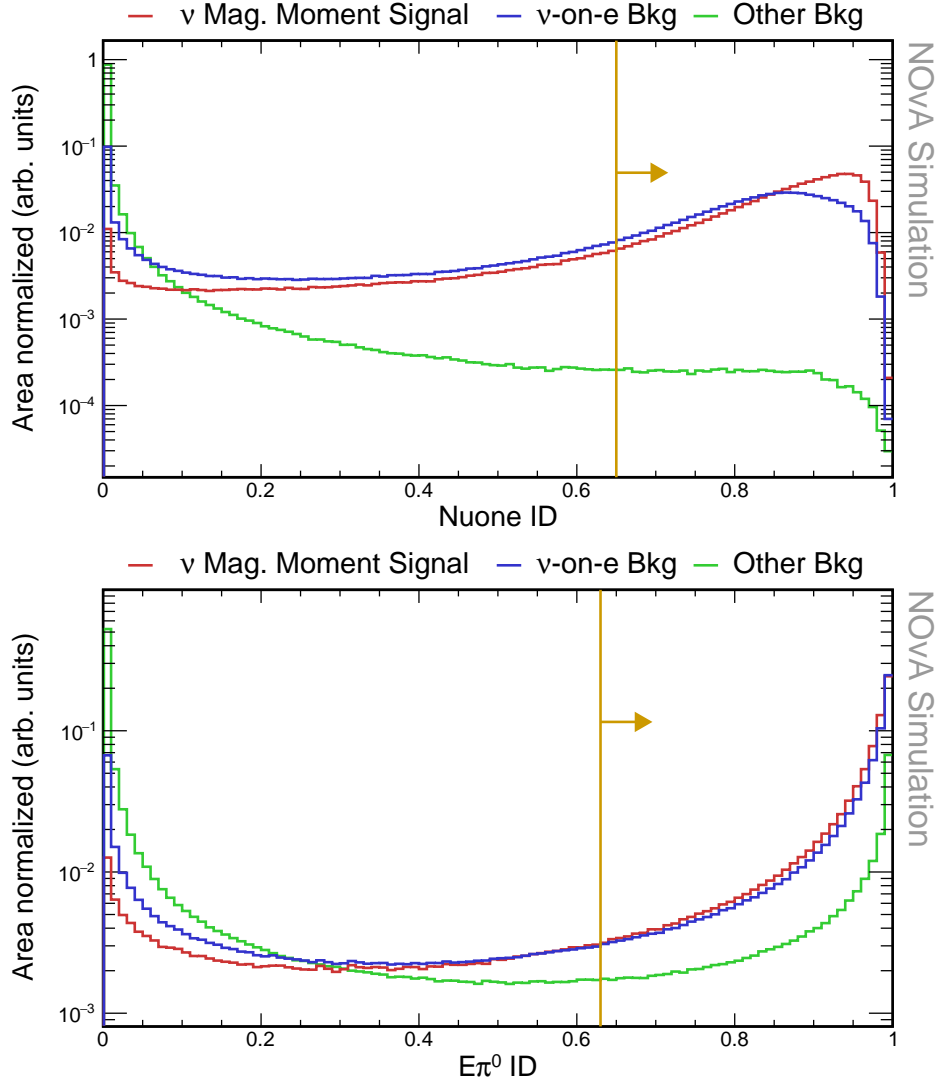


Figure 1.23: Relative comparison of signal (red),  $\nu$ -on-e background (blue), and other background (green) events in the distribution of the NuoneID (top) and  $E\pi^0$ ID (bottom) event identifiers. All histograms are area-normalized and logarithmic in the y axis. The reconstruction quality, pre-selection, fiducial and containment cuts were applied prior to making these plots. Yellow lines show the cut values on the depicted variables, with arrows pointing towards the preserved events.

Also,

$$\frac{\text{Signal}}{\sqrt{\text{Background}}} = 2.15 \quad (1.54)$$

and

$$\text{FOM} = \frac{\text{Signal}}{\sqrt{\text{Signal}+\text{Background}}} = 2.06. \quad (1.55)$$

## 1.4 Systematic Uncertainties

We consider all the standard NOvA systematic uncertainties described in Sec. ??, grouped into four categories: neutrino flux, detector calibration, detector modelling, and neutrino interaction systematic uncertainties. Summary of the effects of both

Table 1.6: Event selection cutflow table for the results of the cut-based Multivariate analysis, showing the number of events and the relative efficiency of each cut for each signal sample. The relative efficiency is calculated as number of events remaining after applying the corresponding cut divided by number of event for all the previous cuts. All the cuts are listed in sequence as they are applied. The top row corresponds to the sample after applying the reconstruction quality, pre-selection, fiducial and containment cuts.

Selection	Signal		$\nu$ -on-e bkg		Other bkg	
	$N_{evt}$	$\epsilon_{rel} (\%)$	$N_{evt}$	$\epsilon_{rel} (\%)$	$N_{evt}$	$\epsilon_{rel} (\%)$
<b>Contained</b>	117.41	100	$2.08 \times 10^3$	100	$1.10 \times 10^6$	100
$E_{Shower}/E_{Tot}$	113.03	96.28	$2.02 \times 10^3$	97.32	$4.53 \times 10^5$	41.30
<b>N<sup>o</sup> Hits</b>	106.48	94.20	$1.45 \times 10^3$	71.53	$4.02 \times 10^5$	88.78
<b>High <math>E_{Shower}</math></b>	85.51	80.31	777.91	53.76	$3.01 \times 10^5$	74.84
<b><math>\nu</math>-on-e ID</b>	72.23	84.47	652.32	83.86	$4.40 \times 10^3$	1.46
<b><math>E\pi^0</math> ID</b>	67.35	93.24	608.19	93.23	$2.83 \times 10^3$	64.34
$E\theta^2$	56.80	84.33	519.09	85.35	181.24	6.40

Table 1.7: Interaction types contributing to the SM background after full event selection. Interactions with/without  $\pi^0$  in the final state are specifically selected due to their significant contribution to the  $\nu$ -on-e background.

Interaction	Number of events
$\nu$ -on-e	519.09
NC w/ $\pi^0$	72.96
NC w/o $\pi^0$	21.51
$\nu_\mu$ CC w/ $\pi^0$	28.07
$\nu_\mu$ CC w/o $\pi^0$	25.67
$\nu_e$ CCMEC	2.22
Other $\nu_e$ CC	9.83
Other	20.98
<b>Total</b>	<b>700.33</b>

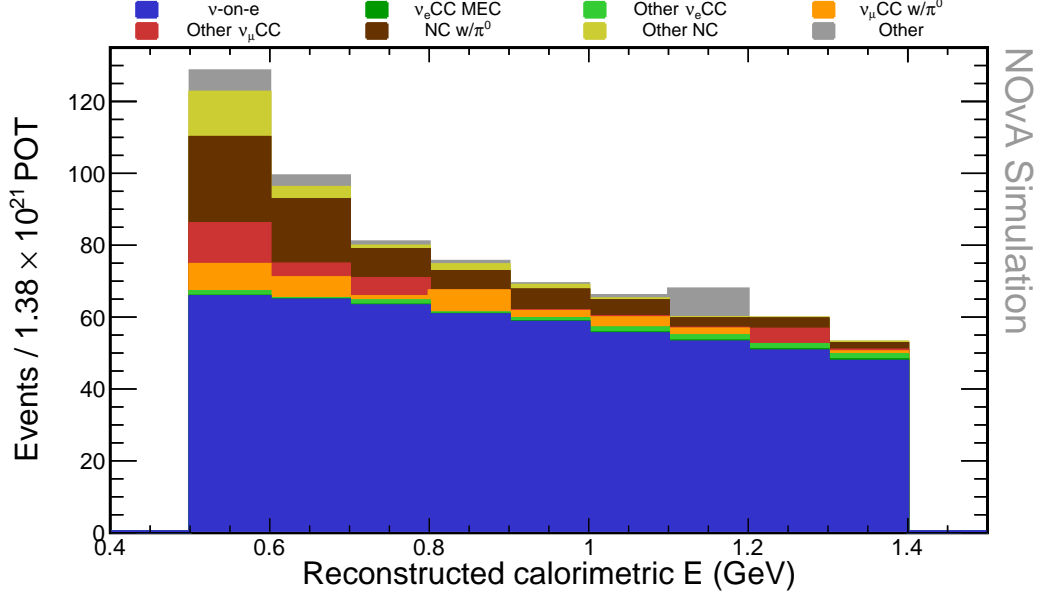


Figure 1.24: Background composition of events passing the full event selection as a function of the reconstructed energy of the leading shower - electron for  $\nu$ -on-e events. Events are scaled to the data exposure. Origin of the "Other" background events between 1.1 – 1.2 GeV is not known.

systematic and statistical uncertainties on the predicted number of SM background events is shown in Fig. 1.25. The four categories of systematic uncertainties are assumed to be uncorrelated between each other, allowing to calculate their combined effect by adding their individual contribution in quadrature. The total prediction of the number of SM background events can be expressed as

$$N_{SM} = 700.33 \pm 26.46 \text{ (stat.)}^{+72.48}_{-62.99} \text{ (syst.)} . \quad (1.56)$$

To assess the effect of the neutrino flux systematic uncertainty, we use 8 ND-only principal components. Figure 1.26 shows their combined effect on the predicted SM background as a function of the primary shower's reconstructed energy. Since the principal components are uncorrelated by construction, the total systematic uncertainty for each bin is calculated by adding the effect of all the principal components in quadrature. The effect of the neutrino flux systematic uncertainty does not depend on the primary shower's calorimetric energy and altering the neutrino flux prediction can be represented by a normalization shift. The final effect of the neutrino flux systematic uncertainty on the total number of SM background events is  $\pm 8.16\%$  and is symmetric around the nominal prediction.



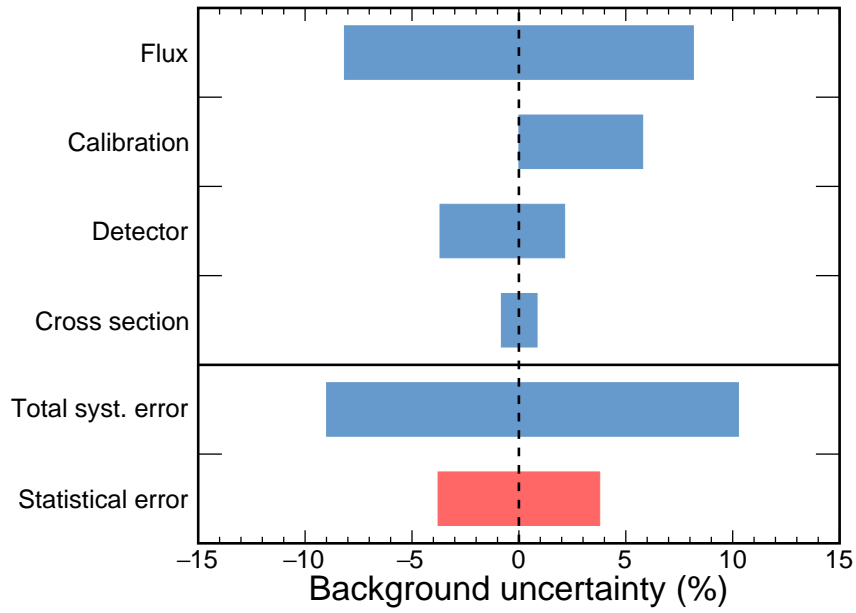


Figure 1.25: Relative effect of systematic and statistical uncertainties on the number of SM background events. The total systematic uncertainty (blue bottom bar) is calculated as a square root of the sum of squares of the four categories of systematic uncertainties, shown ordered by the size of their effect. These are the neutrino flux, detector calibration, detector modelling, and neutrino cross section systematic uncertainties.

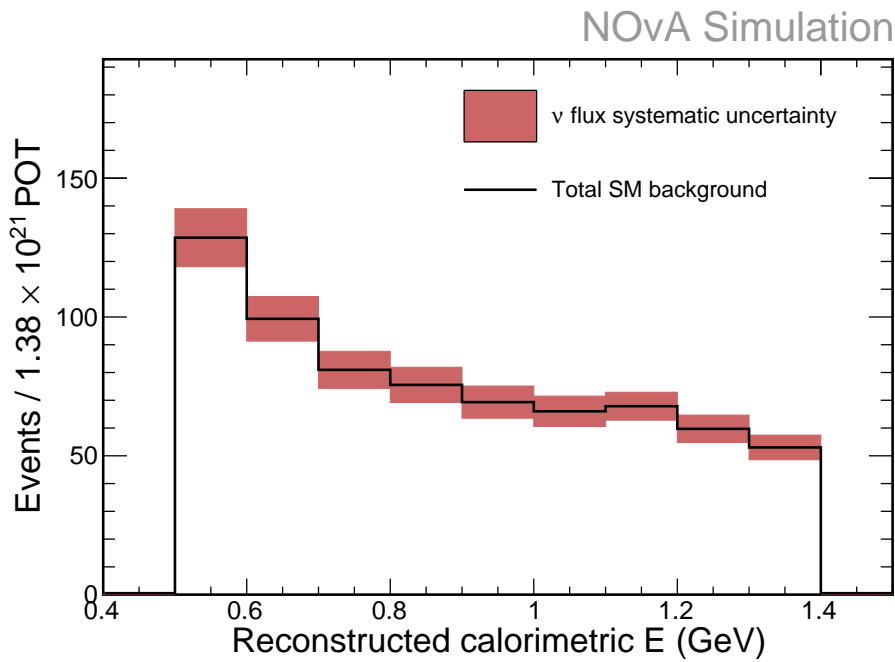


Figure 1.26: Effect of the total neutrino flux systematic uncertainty on the primary shower energy distribution of the SM background events.

The effect of the total detector modelling and calibration systematic uncertainties on the number of SM background events is asymmetrical, increasing the number of events by +6.17 % and decreasing by 3.69 %. The effect of these uncertainties depends on the energy of the primary shower (which is the recoil electron for  $\nu$ -on-e events), as can be seen in Fig. 1.27. This means that the energy distribution of the SM background events can be significantly altered due to the detector uncertainties. The largest contribution comes from the absolute energy scale uncertainty, which has a one-sided effect of +5.72 %. This is due to both the positive and the negative shift in the absolute energy scale increasing the total number of SM background events. The light level and Cherenkov systematic uncertainties are asymmetrical and alter the number of SM background events in both directions by  $+1.13\%$  and  $-3.39\%$  and  $+1.82\%$  and  $-1.46\%$  respectively. The detector ageing and calibration shape systematic uncertainties are one sided by default and increase the number of the SM background events by +0.55 % and +0.69 % respectively.

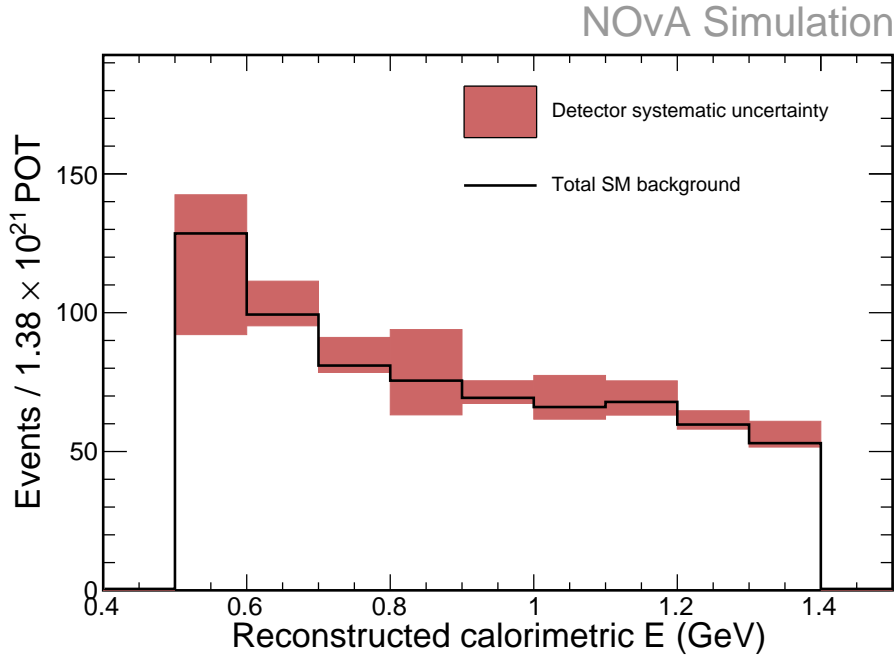


Figure 1.27: Effect of the total detector systematic uncertainty on the primary shower energy distribution of the SM background. The detector uncertainty consists of the absolute calibration, calibration shape, detector ageing, light level, and Cherenkov systematic uncertainties.

Since we assume that the  $\nu$ -on-e interaction is known precisely, the dominant  $\nu$ -on-e component of the SM background has no systematic uncertainty from neutrino interactions. Therefore, the neutrino interaction systematic uncertainty affects

only the 181 "Other background" events, which make up 34.9 % of the total SM background. Consequently, the total neutrino interaction uncertainty on the SM background is relatively small, with a combined effect on the number of SM background events of  $^{+1.54\%}_{-1.49\%}$ . The most dominant neutrino interaction systematic uncertainties are related to interactions with  $\pi^0$  in the final state, such as the axial mass ( $^{+0.97\%}_{-0.90\%}$ ) and the vector mass ( $^{+0.41\%}_{-0.35\%}$ ) of the NCResonant baryon production (Res) interactions, the scaling of the Coherent  $\pi$  (COH $\pi$ )NC interactions ( $^{+0.85\%}_{-0.85\%}$ ), or the mean free path of pions before they undergo an interaction ( $^{+0.30\%}_{-0.43\%}$ ). Other neutrino interaction systematic uncertainties have only a marginal ( $< 0.3\%$ ) effect on the number of SM background events.

## 1.5 Results

As discussed in Sec. 1.3 and Sec. 1.4, the total number of the expected SM background events scaled to the data exposure of  $1.38 \times 10^{21}$  POT is

$$E_B = 700.33 \pm 26.46 \text{ (stat.)}^{+72.48}_{-62.99} \text{ (syst.)} \quad (1.57)$$

The number of expected signal events depends on the size of the neutrino magnetic moment and can be expressed as

$$E_S = 56.80 \times \left( \frac{\mu_\nu}{10^{-9} \mu_B} \right)^2. \quad (1.58)$$

To avoid biasing our decisions based on the observed number of data events and on their distribution, we performed the event selection, systematic uncertainty studies and decided on the statistical analysis methods prior to revealing the data samples in a blinded analysis. Therefore, in the following section, the methodology, the confidence level, and the hypothesis exclusion requirements have been fixed before we unveiled the data sample.

The total number of observed events passing our selection is

$$O = 773. \quad (1.59)$$

The Best Fit (BF) point for the number of signal events can be calculated as

$$BF_S = O - E_B = 72.67 \quad (1.60)$$

and from Eq. 1.58 we get the best fit for the neutrino magnetic moment

$$\mu_{\nu,BF} = \sqrt{\frac{72.67}{56.80}} \times 10^{-9} \mu_B = 1.13 \times 10^{-9} \mu_B \quad (1.61)$$

The final distribution of the predicted SM background, the signal for  $\mu_{\nu} = 10^{-9} \mu_B$  and the measured data in the primary shower reconstructed calorimetric energy is shown in Fig. 1.28. We do not use the energy distribution of events, but we are using this distribution to cross check the validity of our analysis. It appears that everything is grand. The data appears to be within the systematic and statistical uncertainty for all the displayed bins. The only exception is the bin within (0.9 GeV, 1.0 GeV), which is however still within two standard variations from the accepted values and therefore can be safely ignored.

Describe the likelihood ratio in general here We want to maximize the likelihood as a function of the measured parameter. This is equivalent to minimizing the log likelihood ratio as prescribed by...

Likelihood is the probability to observe  $O$  events given a hypothesis  $H$ , which describes the number of expected events  $E$ . In case of the null hypothesis ( $H_0$ ), which states that there is not neutrino magnetic moment and all the observed events are due to the SM, the expected number of events is equivalent to  $E_B$ . As we are counting the number of events recorded in a fixed time interval, the likelihood is described by the Poisson distribution

$$\mathcal{L}(O; \mu) = \frac{E(\mu)^O}{O!} e^{-E(\mu)}. \quad (1.62)$$

When using maximum likelihood [with binned data], one can find the maximum likelihood estimators and at the same time obtain a statistic usable for a test of goodness-of-fit. Maximizing the likelihood  $L(\theta) = f_P(n; \theta)$  is equivalent to maximizing the likelihood ratio  $\lambda(\theta) = f_P(n; \theta) / f(n; \hat{\mu})$ . Equivalently one often minimizes the quantity  $-2 \ln \lambda(\theta)$ . [20]

A smaller value of  $-2 \ln \lambda(\hat{\theta})$  corresponds to better agreement between the data

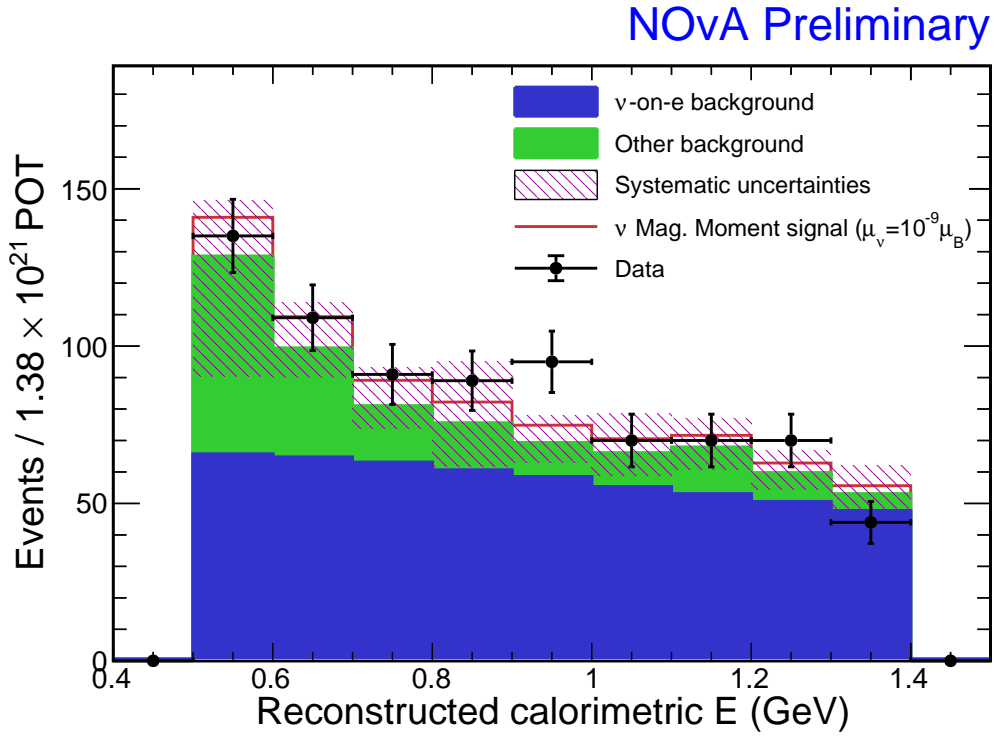


Figure 1.28: Comparison of the observed data to the prediction of the  $\nu$  magnetic moment signal for  $\mu_\nu = 10^{-9} \mu_B$  (red line) and the SM background (filled area) as a function of the reconstructed calorimetric energy of the most energetic shower. The SM background is divided into the  $\nu$ -on-e component in blue and the rest in green, with the associated systematic uncertainty on the SM background shown in shaded purple. Data is shown with statistical uncertainty based on Poisson distribution. All samples are scaled to the true data exposure  $1.38 \times 10^{21}$  POT.

and the hypothesized form of  $\mu(\theta)$ . The value of  $-2 \ln \lambda(\hat{\theta})$  can thus be translated into a **p-value as a measure of goodness-of-fit**. Assuming the model is correct, then according to **Wilk's theorem**, for **sufficiently large**  $\mu_i$  and provided certain regularity conditions are met, **the minimum of  $-2 \ln \lambda$  follows a  $\chi^2$  distribution**. If there are  $N$  bins and  $M$  fitter parameters, then the number of degrees of freedom for the  $\chi^2$  distribution is  $N - M$  if the data are treated as Poisson distributed - which they are for us.

Wilk's theorem [35]

We can include the effect of systematic uncertainties as nuisance parameters into the likelihood function, which can be described by a normal distribution centred around 0, with standard deviation corresponding to the  $1\sigma$  value of the systematic uncertainty. As discussed above, we assume that systematic uncertainties are mutually uncorrelated.

[Nitish's thesis] This prediction is fit to the NuMI data using the traditional Poisson log-likelihood for binned spectra [36]. This is given as:

$$-2 \ln \lambda(\theta, \vec{\eta}) = -2 \sum_{i=1}^N \left[ \mu_i(\theta, \vec{\eta}) - n_i + n_i \ln \frac{n_i}{\mu_i(\theta, \vec{\eta})} \right] + \sum_{k=1}^M \eta_k^2, \quad (1.63)$$

where  $\mu_i$  denotes the predicted number of events in each analysis bin  $i$  as a function of the neutrino magnetic moment  $\theta$  and the nuisance parameters  $\eta$ , which for us are the systematic shifts.  $n_i$  is the observed number of events in that bin. The last term denotes the penalty given to favouring a non-zero systematic variation for  $M$  set of systematic uncertainties. The best-fit oscillation parameters are derived by minimizing this equation with respect to these parameters and is done using a MIGRAD based algorithm [125]. The likelihood takes into account the Poisson deviations of the prediction from data in each analysis bin (given by the  $\ln$  term) as well as an overall Poisson fluctuation on the total number of predicted events. ...the penalty is calculated for the amount of  $\sigma$  deviation favoured in the fit, i.e if the fit favours a  $1.2\sigma$  deviation from the central value prediction then the penalty to  $-2 \ln \lambda$  is given by  $1.2^2 = 1.44$ . The parametrisation is derived by defining the variation in the prediction at specific  $\sigma$  values, for example:  $-2, -1, 0, +1, +2\sigma$  and interpolating the deviations in each analysis bin using a cubic spline-based method. This is sufficiently general for all

the systematics considered in the analysis, including those with non-Gaussian uncertainties. For one-sided systematic shifts the interpolation parametrizes the overall deviation by fitting a flat line at 0 for the excluded shifts and only uses the included shifts.

The log-likelihood form also requires that individual systematic uncertainties are not correlated to each other. This is somewhat justifiable for uncertainties coming from completely separate parts of the simulation for example the flux vs cross-section.

Using all of the parameters  $(\theta, \nu)$  to find the statistical errors in the parameters of interest  $\theta$  is equivalent to using the *profile likelihood*, which depends only on  $\theta$ . It is defined as

$$L_p(\theta) = L(\theta, \hat{\nu}(\theta)), \quad (1.64)$$

This equation is supposed to have double hat for the neutrino on RHS but that throws an error when compiling... where the double-hat notation indicates the profiled values of the parameters  $\nu$ , defined as values that maximize  $L$  for the specified  $\theta$ .

We want to test the (null) hypothesis that the observed number of events can be described by the SM alone, without the presence of any neutrino magnetic moment ( $\mu_\nu = 0$ ). For this we use the likelihood ratio test statistic, which is expressed as a ratio between the maximum likelihood of obtaining the observed data given the SM only, and the maximum likelihood of obtaining the observed data given there the best fit value to the neutrino magnetic moment:

$$\lambda = \frac{\mathcal{L}(\mu_\nu = 0)}{\mathcal{L}(\mu_\nu = \mu_{\nu, BF})}. \quad (1.65)$$

For the null hypothesis, the expected number of events is  $E_B$  and for the alternative hypothesis at the BF point the expected number of events is equal to  $O$ . Additionally, the likelihood ratio is expressed as the logarithm of the ratio, which according to the Wilk's theorem follows the  $\chi^2$  distribution. It can be expressed as

$$-2 \ln \lambda(\theta) = -2 \ln \left( \frac{\mathcal{L}(O; E = E_B)}{\mathcal{L}(O; E = O)} \right) = 2 \left[ E_B - O + O \ln \frac{O}{E_B} \right] \quad (1.66)$$

The minimum log likelihood for our null hypothesis is 1.02964, which corresponds to a double sided p-value of 0.31, or one-sided p-value of 0.16, which is larger than 0.1, therefore we are not able to reject the null hypothesis. Therefore we are putting

a limit on the neutrino magnetic moment parameter of  $\mu_\nu < 1.91 \times 10^{-9} \mu_B$  at 90% C.L., as shown in Fig... This limit is stricter than the current world leading limit. However, there are several possible improvement that could improve our analysis. We can also estimate the systematic uncertainty on the best fit point by taking the  $1\sigma$  range ( $\chi^2 = 1$ ) of the full systematic uncertainty distribution from Fig. 1.29. The  $1\sigma$  range for all systematics is  $(0.14, 1.63) \times 10^{-9} \mu_B$ , which is equivalent to the best fit point having an uncertainty  $\mu_{\nu,BF} = (1.13^{+0.50}_{-0.99}) \times 10^{-9} \mu_B$ .

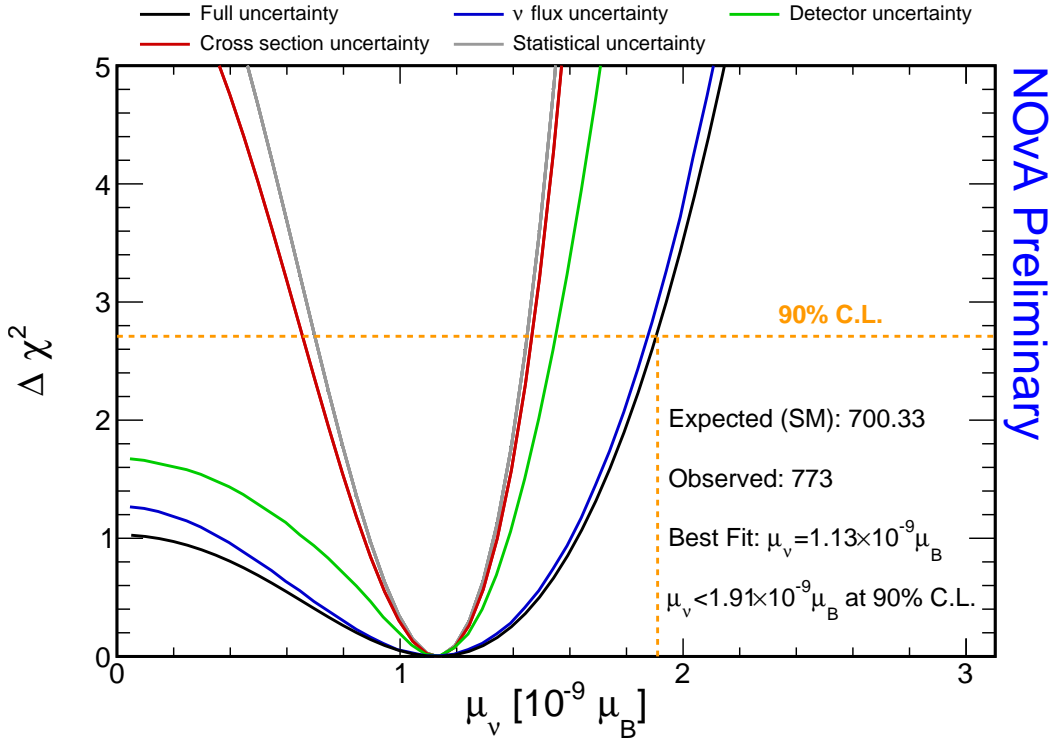


Figure 1.29: Results of the fit of the prediction to the observed data, with the neutrino magnetic moment as the sole fit parameter. We are profiling over the full range of systematic uncertainties.

## 1.6 Discussion

What should be included here:

- Interpretation: Interpret the results in the context of the current understanding of neutrino physics.
- Implications: Explain the broader implications of your findings for the field of particle physics.



- Future work: Suggest directions for future research based on your results.
  - Improvements in NOvA, more FHC data, including RHC data, better reconstruction, better simulation and calibration, better event selection, including sideband samples, more systematics studies, better fitting techniques...
  - Future beyond NOvA - DUNE
    - \* What are the possibilities for DUNE?

If we do an energy dependent fit, we would have to consider the energy dependency of the systematic uncertainties, which might substantially impact the results of this analysis. Same applies if we decide to extend the event selection to lower electron energies below 0.5GeV.

Due to the energy dependent contribution of the NC interactions with a  $\pi^0$  in the final state, it may be important to consider these uncertainties for an energy dependent analysis.

## 1.7 Summary

Summarize the results and compare them to the introduction, including comparisons to other experiments and theory. Restate the significant of the measurement

Closing remarks



# Acronyms

- $\nu$ -on-e** neutrino-on-electron (interaction). [1](#), [2](#), [4](#), [8–17](#), [19–27](#), [30–45](#), [47](#), [50](#)
- APD** Avalanche Photodiode. [20](#)
- BF** Best Fit. [49](#), [52](#), [53](#)
- BSM** Beyond Standard Model. [1–3](#), [5](#), [6](#)
- C.L.** Confidence Level. [1](#), [2](#)
- CC** Charged Current. [10](#), [16](#), [17](#), [24](#), [40](#), [44](#)
- CNN** Convolutional Neural Network. [40](#)
- COH $\pi$**  Coherent  $\pi$  (production). [48](#)
- CVN** Convolutional Visual Network. [19](#), [20](#)
- DCM** Data Concentration Module. [18](#)
- FEB** Front End Board. [20](#)
- FOM** Figure Of Merit. [18](#), [28–38](#), [40](#), [44](#)
- LDM** Light Dark Matter. [2](#)
- MC** Monte Carlo. [15](#), [39](#)
- MEC** Meson Exchange Current. [16](#), [17](#), [44](#)
- ML** Machine Learning. [20](#)
- MVA** Multi Variate Analysis. [17](#), [28](#), [29](#), [57](#)
- NC** Neutral Current. [44](#), [48](#), [54](#)
- ND** Near Detector. [1](#), [2](#), [4](#), [7](#), [14](#), [17](#), [24](#), [28](#), [45](#)
- NOvA** NuMI Off-axis  $\nu_e$  Appearance (experiment). [viii](#), [1](#), [2](#), [4](#), [7](#), [9](#), [11–14](#), [16](#), [17](#), [20](#), [24](#), [39](#), [40](#), [44](#)

**NP** New Physics. [6](#)

**NuMI** Neutrinos from the Main Injector. [28](#)

**PMNS** Pontecorvo-Maki-Nakagawa-Sakata. [5](#), [6](#)

**POT** Protons On Target. [14](#), [16](#), [18](#), [23](#), [48](#), [50](#)

**PPFX** Package to Predict the Flux. [14](#)

**Res** Resonant baryon production. [48](#)

**SM** Standard Model. [1](#), [3–6](#), [10–15](#), [18](#), [40](#), [44–50](#), [52](#)

**TMVA** Tool for MVA. [29](#), [39](#), [40](#)

# Bibliography

- [1] Patrick Huber et al. Snowmass Neutrino Frontier Report. In *Snowmass 2021*, 11 2022.
- [2] E. Aprile et al. Excess electronic recoil events in XENON1T. *Phys. Rev. D*, 102: 072004, . doi:[10.1103/PhysRevD.102.072004](https://doi.org/10.1103/PhysRevD.102.072004).
- [3] E. Aprile et al. Search for New Physics in Electronic Recoil Data from XENONnT. *Phys. Rev. Lett.*, 129:161805, . doi:[10.1103/PhysRevLett.129.161805](https://doi.org/10.1103/PhysRevLett.129.161805).
- [4] M. Atzori Corona, W. M. Bonivento, M. Cadeddu, N. Cargioli, and F. Dordei. New constraint on neutrino magnetic moment and neutrino millicharge from LUX-ZEPLIN dark matter search results. *Phys. Rev. D*, 107:053001. doi:[10.1103/PhysRevD.107.053001](https://doi.org/10.1103/PhysRevD.107.053001).
- [5] M. Agostini et al. Limiting neutrino magnetic moments with Borexino Phase-II solar neutrino data. *Phys. Rev. D*, 96:091103. doi:[10.1103/PhysRevD.96.091103](https://doi.org/10.1103/PhysRevD.96.091103).
- [6] Amir N. Khan. Light new physics and neutrino electromagnetic interactions in XENONnT. *Physics Letters B*, 837:137650. ISSN 0370-2693. doi:[10.1016/j.physletb.2022.137650](https://doi.org/10.1016/j.physletb.2022.137650). URL <https://www.sciencedirect.com/science/article/pii/S0370269322007845>.
- [7] K. S. Babu, Sudip Jana, and Manfred Lindner. Large Neutrino Magnetic Moments in the Light of Recent Experiments. *JHEP*, 10:040. doi:[10.1007/JHEP10\(2020\)040](https://doi.org/10.1007/JHEP10(2020)040).
- [8] L. B. Auerbach et al. Measurement of electron-neutrino electron elastic scattering. *Phys. Rev. D*, 63:112001. doi:[10.1103/PhysRevD.63.112001](https://doi.org/10.1103/PhysRevD.63.112001).
- [9] D. A. Krakauer et al. Limits on the neutrino magnetic moment from a measurement of neutrino - electron elastic scattering. 252:177–180. doi:[10.1016/0370-2693\(90\)91100-P](https://doi.org/10.1016/0370-2693(90)91100-P).
- [10] L. A. Ahrens et al. Determination of electroweak parameters from the elastic scattering of muon neutrinos and antineutrinos on electrons. *Phys. Rev. D*, 41: 3297–3316, Jun 1990. doi:[10.1103/PhysRevD.41.3297](https://doi.org/10.1103/PhysRevD.41.3297).

- [11] P. Vilain et al. Experimental study of electromagnetic properties of the muon-neutrino in neutrino - electron scattering. *Phys. Lett. B*, 345:115–118, 1995. doi:[10.1016/0370-2693\(94\)01678-6](https://doi.org/10.1016/0370-2693(94)01678-6).
- [12] Biao Wang. *Muon-Neutrino Electron Elastic Scattering and a Search for the Muon-Neutrino Magnetic Moment in the NOvA Near Detector*. PhD thesis. URL [https://scholar.smu.edu/hum\\_sci\\_physics\\_etds/1](https://scholar.smu.edu/hum_sci_physics_etds/1).
- [13] Wenjie Wu and Yiwen Xiao. Constraint of the Integrated Neutrino Flux from Neutrino-Electron Elastic Scattering in the NOvA Near Detector. NOVA Document 56383. URL <https://nova-docdb.fnal.gov/cgi-bin/sso/ShowDocument?docid=56383>. NOvA technical note.
- [14] Athula Wickremasinghe, Wenjie Wu, and Yiwen Xiao. Status of the Measurement of Neutrino-Electron Elastic Scattering in the NOvA Near Detector. In *Neutrino 2022*. URL <https://indico.kps.or.kr/event/30/contributions/738/>.
- [15] Barnali Brahma, Tyler Horoho, and Mu Wei. TechNote: Light Dark Matter Search with NOvA Near Detector. NOVA Document 59439. URL <https://nova-docdb.fnal.gov/cgi-bin/sso/ShowDocument?docid=59439>. NOvA technical note.
- [16] Carlo Giunti and Alexander Studenikin. Neutrino electromagnetic interactions: A window to new physics. *Rev. Mod. Phys.*, 87:531–591, Jun 2015. doi:[10.1103/RevModPhys.87.531](https://doi.org/10.1103/RevModPhys.87.531).
- [17] Boris Kayser. Majorana neutrinos and their electromagnetic properties. *Phys. Rev. D*, 26:1662–1670, Oct 1982. doi:[10.1103/PhysRevD.26.1662](https://doi.org/10.1103/PhysRevD.26.1662).
- [18] José F. Nieves. Electromagnetic properties of majorana neutrinos. *Phys. Rev. D*, 26:3152–3158, Dec 1982. doi:[10.1103/PhysRevD.26.3152](https://doi.org/10.1103/PhysRevD.26.3152).
- [19] Carlo Giunti, Julieta Gruszko, Benjamin Jones, Lisa Kaufman, Diana Parno, and Andrea Pocar. Report of the Topical Group on Neutrino Properties for Snowmass 2021. 9 2022.
- [20] R. L. Workman and Others. Review of Particle Physics. *PTEP*, 2022:083C01, 2022. doi:[10.1093/ptep/ptac097](https://doi.org/10.1093/ptep/ptac097).

- [21] Nicole F. Bell, Mikhail Gorchtein, Michael J. Ramsey-Musolf, Petr Vogel, and Peng Wang. Model independent bounds on magnetic moments of Majorana neutrinos. *Phys. Lett. B*, 642:377–383, 2006. doi:[10.1016/j.physletb.2006.09.055](https://doi.org/10.1016/j.physletb.2006.09.055).
- [22] Nicole F. Bell, Vincenzo Cirigliano, Michael J. Ramsey-Musolf, Petr Vogel, and Mark B. Wise. How magnetic is the Dirac neutrino? *Phys. Rev. Lett.*, 95:151802, 2005. doi:[10.1103/PhysRevLett.95.151802](https://doi.org/10.1103/PhysRevLett.95.151802).
- [23] M.C. Gonzalez-Garcia and Michele Maltoni. Phenomenology with Massive Neutrinos. *Phys. Rept.*, 460:1–129, 2008. doi:[10.1016/j.physrep.2007.12.004](https://doi.org/10.1016/j.physrep.2007.12.004).
- [24] Carlo Giunti and Chung W. Kim. *Fundamentals of Neutrino Physics and Astrophysics*. 2007. ISBN 978-0-19-850871-7.
- [25] P. Vogel and J. Engel. Neutrino electromagnetic form factors. *Phys. Rev. D*, 39:3378–3383, Jun 1989. doi:[10.1103/PhysRevD.39.3378](https://doi.org/10.1103/PhysRevD.39.3378).
- [26] M. A. Acero et al. Improved measurement of neutrino oscillation parameters by the NOvA experiment. *Phys. Rev. D*, 106(3):032004, 2022. doi:[10.1103/PhysRevD.106.032004](https://doi.org/10.1103/PhysRevD.106.032004).
- [27] E. Valencia et al. Constraint of the MINERνa medium energy neutrino flux using neutrino-electron elastic scattering. *Phys. Rev. D*, 100:092001, Nov 2019. doi:[10.1103/PhysRevD.100.092001](https://doi.org/10.1103/PhysRevD.100.092001).
- [28] Jens Erler and Shufang Su. The weak neutral current. 71:119–149. ISSN 0146-6410. doi:[10.1016/j.pnpnp.2013.03.004](https://doi.org/10.1016/j.pnpnp.2013.03.004). URL <https://www.sciencedirect.com/science/article/pii/S0146641013000239>. Fundamental Symmetries in the Era of the LHC.
- [29] D.Yu Bardin and V.A. Dokuchaeva. On one-loop electroweak corrections to neutrino-electron elastic scattering. 246(2):221–230. ISSN 0550-3213. doi:[10.1016/0550-3213\(84\)90293-1](https://doi.org/10.1016/0550-3213(84)90293-1). URL <https://www.sciencedirect.com/science/article/pii/0550321384902931>.
- [30] Teresa Lackey. Data Quality Technical Note Prod5.1/2023. NOVA Document 59876. URL <https://nova-docdb.fnal.gov/cgi-bin/sso/ShowDocument?docid=59876>. NOvA technical note.

- [31] Erin Ewart. Primary and Secondary Vertexing Update for February 2024 Collaboration Meeting. NOVA Document 61190, February 2024. URL <https://nova-docdb.fnal.gov/cgi-bin/sso/ShowDocument?docid=61190>. NOvA internal document.
- [32] Leonidas Aliaga, Derek Doyle, Matthew Judah, Norm Buchanan, Linda Cremonesi, Mat Muether, and Jon Paley. Measurement of the Double-Differential Inclusive Electron-Neutrino Charged-Current Cross Section in the NOvA Near Detector. NOVA Document 37668, 04 2020. URL <https://nova-docdb.fnal.gov/cgi-bin/sso/ShowDocument?docid=37668>. NOvA technical note.
- [33] Rene Brun et al. root-project/root: v6.22/08. URL <https://doi.org/10.5281/zenodo.3895860>.
- [34] Andreas Hoecker, Peter Speckmayer, Joerg Stelzer, Jan Therhaag, Eckhard von Toerne, and Helge Voss. TMVA: Toolkit for Multivariate Data Analysis. *PoS, ACAT:040*, 2007.
- [35] S. S. Wilks. The Large-Sample Distribution of the Likelihood Ratio for Testing Composite Hypotheses. *Annals Math. Statist.*, 9(1):60–62, 1938. doi:[10.1214/aoms/1177732360](https://doi.org/10.1214/aoms/1177732360).
- [36] Roger Barlow. Extended maximum likelihood. 297(3):496–506. ISSN 0168-9002. doi:[10.1016/0168-9002\(90\)91334-8](https://doi.org/10.1016/0168-9002(90)91334-8). URL <https://www.sciencedirect.com/science/article/pii/0168900290913348>.